


Fringe field maps for symplectic models of general Cartesian dipolesRyan Lindberg^{*} and Michael Borland[†]*Advanced Photon Source, Argonne National Laboratory, Argonne, Illinois 60439, USA* (Received 29 August 2023; accepted 26 October 2023; published 21 November 2023)

We present a framework with which to analyze the effects of magnetic fringe fields. The theory defines the fringe field to be the transition between two regions of nearly constant field, and can incorporate constant multipoles in the magnet body. We then analyze Cartesian dipoles and derive symplectic fringe field maps that are applicable to longitudinal and/or transverse gradient dipoles. We verify the fringe maps with tracking, and show how we incorporated the theory into the tracking code `ELEGANT`. The resulting elements and several supporting scripts are now available for users, and we conclude with several predictions relevant to the APS Upgrade project.

DOI: [10.1103/PhysRevAccelBeams.26.114001](https://doi.org/10.1103/PhysRevAccelBeams.26.114001)**I. INTRODUCTION**

Particle tracking for accelerators typically treats magnets using hard edge models, wherein the magnetic lattice is composed of a sequence of piece-wise continuous regions that have constant multipole content. The hard edge approximation allows for fast, symplectic tracking, since the numerical step size is dictated by the size and strength of the magnets themselves, and explicit integration methods are possible using splitting techniques. While the hard edge idealization provides a good starting point for lattice design, real magnets have multipole fields that transition from zero to their nearly constant values over a finite length. These transition regions contain the magnet fringe fields, and the fringe fields can give rise to additional focusing that can change the tune, and nonlinear contributions that can modify, for example, the chromaticity. Hence, we would like to have a simple way to include the fringe field effects while retaining all the advantages of the standard hard edge tracking.

Calculating fringe field effects in dipoles has a long history, with the definitive reference probably still being the second order results by Brown [1]. Since that time, Ref. [2] extended the calculation to higher order, while the relatively recent work of [3] applied Hamiltonian perturbation theory to extract dipole fringe field maps. Another approach to dipole fringe fields was presented in Ref. [4] and subsequently reviewed in [5], wherein the dipole is

assumed to be sufficiently wide such that the field depends only on the longitudinal and vertical coordinates. We will show how to recover this “infinite parallel face” approximation within our theory, in which case our analysis agrees with the results of [4]. Additionally, we will indicate under what conditions our approach can be reconciled with the quite different predictions presented in, e.g., [6,7].

The goal of this paper is to extend the results of [1] and [3] in essentially three ways. First, we will employ a more general definition of the fringe field that can be applied to longitudinal gradient dipoles used in ultralow emittance lattices [8–10]; second, our model will allow for nonzero quadrupole and/or sextupole content in the magnet body, which will therefore be able to describe either nonideal effects in usual dipoles or the transverse focusing that is designed into transverse gradient dipoles; third, we will show how to employ the resulting fringe field maps as symplectic transformations of the coordinates.

This paper will consider Cartesian dipoles, which are bending magnets that have straight magnet poles. This should be contrasted with sector bends whose poles are swept to follow the design trajectory. The integrated multipole content of Cartesian dipoles is only properly defined with respect to Cartesian coordinates, so that these dipoles are best described using (x, y, z) . Nevertheless, our results will essentially agree with the sector bend calculations of Refs. [1–3] when the dipole has a purely bending field in the magnet body, and also match the parallel plate predictions of Ref. [4]. In this idealization the magnetic fields of Cartesian and sector bends are indistinguishable within the magnet body, so that the difference between sector bends and Cartesian dipoles comes from any non-zero quadrupole, sextupole, or higher order components to the bending field. We will show a few cases from the APS-U [9] where these differences are important, including two reverse-bend dipoles [11,12] designed for the APS-U

^{*}lindberg@anl.gov[†]mborland@anl.gov

Published by the American Physical Society under the terms of the Creative Commons Attribution 4.0 International license. Further distribution of this work must maintain attribution to the author(s) and the published article's title, journal citation, and DOI.

that closely resemble displaced quadrupoles, and a longitudinal gradient dipole designed for the APS-U whose dominant multipole components come from sextupole-like terms.

Our paper is organized as follows. We begin in Sec. II with a general description of the magnetic field, and then present the hard edge model and its associated fringe field. This model is then used in the Hamiltonian perturbation theory of Sec. III, with which we derive symplectic fringe field maps applicable to generic Cartesian dipoles. We compare theoretical predictions to those obtained by tracking in Sec. IV, finding good agreement for both idealized fringe field models and for those designed for the APS-U. In Sec. V we show how the theory was incorporated into the tracking code ELEGANT [13], including some tracking results relevant to the APS-U lattice. Finally, we conclude in Sec. VI.

II. DESCRIPTION OF THE MAGNETIC FIELD

Previous analytic descriptions modeled the fringe field using a curved and inclined boundary [1,2]. This model includes one dipolelike fringe profile that describes the longitudinal variation of the bending field, along with one sextupolelike profile that gives the field curvature associated with a dipole of finite horizontal extent. This model was also adopted in [3], where it was shown to be derivable from the assumption that the field respects rotational symmetry at the boundary. Our approach will instead rely on the generalized gradient representation of the field [14–16]. While the use of generalized gradients may seem to replace geometric considerations with more brute force calculations, in the process it provides a systematic way to include all possible field components. Furthermore, our final results have the advantage that all fringe field integrals that arise in the particle maps can be naturally and accurately computed using tools that compute the generalized gradients from magnetic field data [15–17].

A. Generalized gradient representation

We would like to describe the magnetic field using a representation that both satisfies the vacuum Maxwell equations and expresses the transverse dependence of the field as a Taylor series in the (assumed small) coordinates x and y . This can be done using generalized gradients [14–16], wherein the magnetic field associated with each multipole component is expanded as a series whose coefficients are longitudinal multipolelike field profiles and their derivatives. Our model for the fringe field will include dipole, quadrupole, and sextupole components, and uses a vector potential that is a truncated sum of the associated generalized gradient expansion. We describe these vector potentials and our choice of gauge in this section.

The vector potential describing a magnetic field with no skew components has the generalized gradient expansion

$$(\mathbf{A}, A_z) = \sum_{m=1}^{\infty} (\mathbf{A}^m, A_z^m). \quad (1)$$

The azimuthal dependence of $A_z^m \propto e^{im\phi}$ while $\mathbf{A}^m \propto e^{i(m+1)\phi}$, and each term can be expanded as a Taylor series in the transverse coordinates whose z -dependent coefficients define the generalized gradients and their derivatives. Reference [16] writes this expansion in the symmetric Coulomb gauge as

$$A_z^m(x, y; z) = -\Re[(x + iy)^m] \times \sum_{\ell=0}^{\infty} \frac{(-1)^\ell m! (x^2 + y^2)^\ell}{4^\ell \ell! (\ell + m)!} C_m^{[2\ell]}(z) \quad (2)$$

$$A_x^m(x, y; z) = \frac{1}{2} \Re[(x + iy)^{m+1}] \times \sum_{\ell=0}^{\infty} \frac{(-1)^\ell m! (x^2 + y^2)^\ell}{4^\ell \ell! (\ell + m + 1)!} C_m^{[2\ell+1]}(z) \quad (3)$$

$$A_y^m(x, y; z) = \frac{1}{2} \Im[(x + iy)^{m+1}] \times \sum_{\ell=0}^{\infty} \frac{(-1)^\ell m! (x^2 + y^2)^\ell}{4^\ell \ell! (\ell + m + 1)!} C_m^{[2\ell+1]}(z), \quad (4)$$

where $C_m^{[n]}(z)$ is the n th derivative of $C_m(z)$. When the longitudinal variation is small so too are the transverse components (A_x, A_y), and the longitudinal A_z is given by a sum over the magnetic multipole components.

We will model the fringe field using the $m = 1, 2, 3$ components of the vector potential through fourth order in the particle coordinates. In addition, we will find it convenient to work in the gauge where $A_y = 0$ as suggested by [3], which we set by subtracting from (A_x, A_y, A_z) the following gradient:

$$\nabla \left[\frac{x^3 + 3xy^2}{12} C_1'(z) + \frac{x^4 + 6xy^2 - y^4}{24} C_2'(z) - \frac{2x^5 + 10x^3y^2 + 5xy^4}{480} C_1'''(z) + \frac{x^5 + 10x^3y^2 - 5xy^4}{40} C_3'(z) \right]. \quad (5)$$

Then, to connect with previous work we can introduce the dimensionless on-axis dipole and quadrupole field profiles

$$D(z) = \frac{q\rho}{p_0} C_1(z) \quad Q(z) = \frac{2q}{Kp_0} C_2(z). \quad (6)$$

Here, ρ is the nominal bending radius, K is the nominal focusing gradient, q is the particle charge, and p_0 is the reference momentum. Well inside the body of a transverse gradient dipole both $D(z)$ and $Q(z)$ will approach unity, while each becomes vanishingly small far outside the magnet. The field curvature term is obtained from the following linear combination of the sextupole gradient and the second order derivative of the dipole profile:

$$\frac{1}{\rho B_0} \frac{\partial^2 B_y}{\partial x^2} = -\frac{q}{p_0} \left[\frac{1}{4} C_1''(z) - 6C_3(z) \right]. \quad (7)$$

The quantity in Eq. (7) is related to the curved field boundary introduced by Brown [1] and a similar definition used by [3]; physically it accounts for the finite horizontal extent of the magnet. Our dipole fringe terms will yield the corresponding horizontally infinite result of Lee-Whiting [4] when $24C_3(z) - C_1''(z) \propto \partial_x^2 B_y = 0$, while reproducing the pure $m = 1$ multipole terms of Refs. [6,7] when $C_3 = 0$ and $\partial_x^2 B_y \propto C_1''$. For those interested, Appendix A shows how connect the two-dimensional, parallel face dipole representation described in Refs. [4,5] to our generalized gradient representation at higher order. In any event, we choose to quote all final results in terms of the generalized gradients C_1 , C_2 , C_3 , and their derivatives, so that connections to previous works should be made with the distinctions just highlighted in mind.

Putting everything together, we retain the fourth order terms of the dipole, quadrupole, and sextupole terms of the vector potential (2)–(4), choose the gauge by subtracting the gradient (5), and write the result in terms of the definitions (6) and (7) to obtain

$$A_z = -\frac{p_0}{q} \left[\frac{x}{\rho} D(z) + \frac{x^3 - 3xy^2}{6\rho B_0} \frac{\partial^2 B_y}{\partial x^2} + \frac{x^2 - y^2}{2} KQ(z) - \frac{x^4 - 6x^2y^2 - y^4}{48} KQ''(z) \right] \quad (8)$$

$$A_x = -\frac{p_0}{q} \left[\frac{y^2}{2\rho} D'(z) - \frac{8y^4}{192\rho} D'''(z) + \frac{6x^2y^2 - y^4}{24\rho B_0} \frac{\partial^2 B_y}{\partial x^2} + \frac{xy^2}{2} KQ'(z) \right]. \quad (9)$$

The vector potential (8) and (9) forms the basis for our model of the dipole field. In the next section we introduce its hard-edge approximation. The difference between these two defines the fringe field from which we will derive the corresponding coordinate maps.

B. Hard edge approximation of a bending magnet

We will suppose that there is a boundary between two regions of nearly uniform magnetic field as shown in Fig. 1.

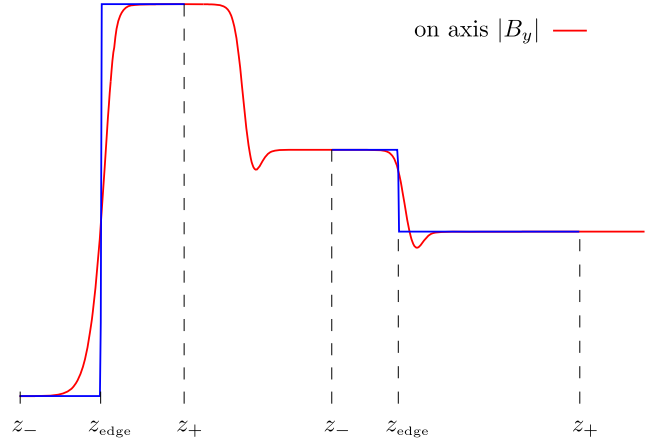


FIG. 1. Example of the on-axis magnetic field profile (red) and the corresponding hard edge models (blue). On the left is the entrance edge geometry where the field starts from zero at z_- and reaches a maximum at z_+ . The hard edge model on the right approximates a longitudinal gradient dipole where the fringe field profile is more complicated.

We assume that far to the left (in the “−” region) the magnetic field is described by an approximately constant bending field and multipoles, and similar conditions are satisfied far to the right (in the “+” region). Importantly, however, the two regions have different multipole content, and are separated by a length over which the field changes. We further suppose that the transition between these two regions occurs over a short distance, such that its effect can be considered within perturbation theory. We then identify the nominal boundary (or hard edge) between the two regions with the coordinate z_{edge} , and finally use z_{\pm} to label coordinates in the \pm -regions that are either far from the edge (if the ideal field in that region is zero) or near the middle of the flat-field region (if $B \neq 0$).

The precise location of z_+ and z_- is not terribly important, since we assume that the field in their vicinity is approximately constant; we can take their location to be at the local maximum of $|B|$ if the magnet is left-right symmetric, or near the center of the flat-field region for cases like that in Fig. 1. The location of the hard edge is important, however, and is defined such that the integrated bending field matches that of its hard edge model.

To be more explicit, we start by describing the hard-edge field profile using the step function

$$\Pi_1(z) = C_1(z_+) \Theta(z - z_{\text{edge}}) + C_1(z_-) \Theta(z_{\text{edge}} - z), \quad (10)$$

where the Heaviside step function $\Theta(z) = 0$ if $z < 0$ and $\Theta(z) = 1$ if $z > 0$. If we are considering the entrance to a magnet as illustrated by the left-hand side of Fig. 1 then all the field components at z_- vanish, while if it is a magnet exit then those at z_+ are zero; the magnetic profile shown on the right-hand side of Fig. 1 has nonvanishing steps at

both z_+ and z_- . We define the hard edge z_{edge} to match the integrated bending field as follows:

$$\begin{aligned} & \int_{z_-}^{z_+} dz B_y(0, 0, z) \\ &= \int_{z_-}^{z_+} dz C_1(z) \\ &= (z_+ - z_{\text{edge}})\Pi_1(z_+) + (z_{\text{edge}} - z_-)\Pi_1(z_-). \end{aligned} \quad (11)$$

The hard edge bending profile defines the nominal bending radius in each region by

$$\frac{1}{\rho_+} = \frac{q}{p_0} \Pi_1(z_+) \quad \text{and} \quad \frac{1}{\rho_-} = \frac{q}{p_0} \Pi_1(z_-), \quad (12)$$

where q is the particle charge and p_0 is the reference momentum. Electrons have $q = -|e|$ and $B_y = \Pi_1(z_+) < 0$ for a positive bending radius.

We have used the dipole field to specify the location of the hard edge step z_{edge} in terms of the reference field locations z_{\pm} . These in turn define the hard edge profiles of the quadrupole and sextupole components via

$$\Pi_2(z) = C_2(z_+)\Theta(z - z_{\text{edge}}) + C_2(z_-)\Theta(z_{\text{edge}} - z) \quad (13)$$

$$\Pi_3(z) = C_3(z_+)\Theta(z - z_{\text{edge}}) + C_3(z_-)\Theta(z_{\text{edge}} - z). \quad (14)$$

Then, for example, the geometric focusing strength in each region is

$$K_+ = \frac{q}{p_0} 2C_2(z_+) \quad \text{and} \quad K_- = \frac{q}{p_0} 2C_2(z_-),$$

with again the caveat that we set $K_{\pm} \rightarrow 0$ in regions far outside the magnet. For pure dipoles we expect $K_{\pm} \approx 0$ in the body as well, but we will make no assumptions as to its size. Hence, our theory will be able to describe both nonideal effects in regular dipoles as well as the strong focusing that is designed into transverse gradient dipoles. The focusing in a well-made transverse gradient dipole should satisfy

$$\frac{q}{p_0} \int_{z_-}^{z_+} dz 2C_2(z) \approx (z_+ - z_{\text{edge}})K_+ + (z_{\text{edge}} - z_-)K_-,$$

but the two may not be equal due to small differences in the fringe field shape of the quadrupole and dipole field components.

III. HAMILTONIAN PERTURBATION THEORY

This section describes how we apply Hamiltonian perturbation theory to construct symplectic maps that account for the effects of dipole fringe fields. Our approach employs the same basic techniques as those used in

Ref. [3], but with three main differences: first, we allow for nonzero quadrupole and sextupole terms in the body; second, we use our more general definition of the hard edge model and its corresponding fringe field; third, we consider the unperturbed motion to be that of the hard edge model in Cartesian coordinates. The last two features eliminate the need to separately calculate the entrance and exit maps, and somewhat streamlines the calculation of the map itself.

Bending magnets with straight poles define integrated multipole content with respect to the straight axis z , and furthermore have hard edges defined by planes of constant z . Hence, our calculations are simplest when expressed using the initial particle coordinates along the hard edge. In our typical accelerator formalism, however, upstream elements deliver particles to the entrance plane shown as the red line in Fig. 2(a), and this entrance plane makes an angle θ with respect to the magnet face shown in blue. In this case we must first drift the particles from the entrance plane to the hard edge of the magnet at $z = 0$. To compute this transformation, we denote the magnitude of the momentum as P_{\parallel} , and use the subscript e for coordinates along the entrance plane and 0 for those at the hard edge. For example, along the entrance plane $P_{\parallel,e}^2 = P_{x,e}^2 + P_{y,e}^2 + P_{z,e}^2$, and since the total momentum is constant we have $P_{\parallel,e} = P_{\parallel,0}$. The transverse momentum components at the hard edge are related to those along the entrance plane by a simple rotation, with

$$\begin{aligned} P_{x,0} &= P_{x,e} \cos \theta + P_{z,e} \sin \theta \\ &= P_{x,e} \cos \theta + \sqrt{P_{\parallel}^2 - P_{x,e}^2 - P_{y,e}^2} \sin \theta \end{aligned} \quad (15)$$

$$P_{y,0} = P_{y,e}. \quad (16)$$

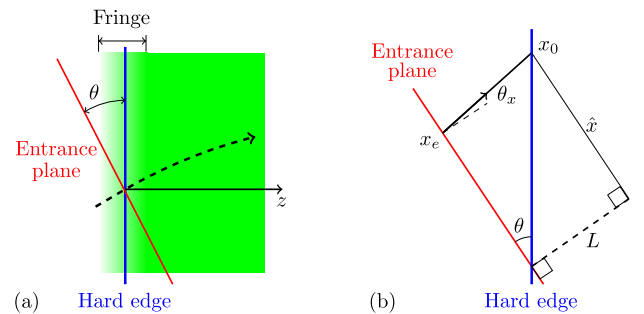


FIG. 2. (a) Basic layout of a straight dipole. The entrance plane in red is at an angle θ from the magnet hard edge in blue. The hard edge is located inside the narrow fringe region where the magnetic field transitions between two values. The reference trajectory is dashed. (b) Geometry relating the horizontal position along the entrance plane x_e to that at the hard edge x_0 . The particle momentum makes the angle θ_x with respect to the entrance plane normal, and is transported a distance L along z_e to the hard edge.

Using simple geometry we also have

$$x_0 = \frac{\hat{x}}{\cos \theta} = \frac{x_e + x'_e L}{\cos \theta} = \frac{x_e + x'_e x_0 \sin \theta}{\cos \theta}, \quad (17)$$

where $x'_e = dx_e/dz_e = \tan \theta_x$ in the rectangular system defined by the entrance plane. Solving for x_0 we find that

$$x_0 = \frac{x_e}{\cos \theta} + \frac{x'_e x_e \tan \theta \sec \theta}{1 - x'_e \tan \theta}. \quad (18)$$

Equation (18) is the sum of the geometric contribution $x_e/\cos \theta$ and an addition corresponding to a drift along z_e by the amount $L = x_0 \sin \theta = x_e \tan \theta / (1 - x'_e \tan \theta)$. The other coordinates are given by $y_0 = y_e + y'_e L$ and $vt_0 = vt_e + vt'_e L$; expressing everything in terms of momenta using $x'_e = P_{x,e}/P_{z,e}$, $y'_e = P_{y,e}/P_{z,e}$, and $vt'_e = P_{\parallel}/P_{z,e}$ implies that

$$x_0 = \frac{x_e}{\cos \theta} + \frac{P_{x,e} x_e \tan \theta \sec \theta}{\sqrt{P_{\parallel}^2 - P_{x,e}^2 - P_{y,e}^2} - P_{x,e} \tan \theta} \quad (19)$$

$$y_0 = y_e + \frac{P_{y,e} x_e \tan \theta}{\sqrt{P_{\parallel}^2 - P_{x,e}^2 - P_{y,e}^2} - P_{x,e} \tan \theta} \quad (20)$$

$$vt_0 = vt_e + \frac{P_{\parallel} x_e \tan \theta}{\sqrt{P_{\parallel}^2 - P_{x,e}^2 - P_{y,e}^2} - P_{x,e} \tan \theta}. \quad (21)$$

One can show that the transformation equations (15)–(21) are symplectic by verifying that

$$\mathbf{M}^T \mathbf{J} \mathbf{M} = \mathbf{J}, \quad (22)$$

where \mathbf{J} is the usual skew-symmetric symplectic matrix and \mathbf{M} is the Jacobian matrix of the transformation:

$$\mathbf{J} = \begin{bmatrix} 0 & \mathbb{I} \\ -\mathbb{I} & 0 \end{bmatrix} \quad \mathbf{M}_{i,j} = \frac{\partial \mathcal{Z}_{0,i}}{\mathcal{Z}_{e,j}}. \quad (23)$$

Here, $\mathcal{Z} = (x, y, -vt, P_x, P_y, P_{\parallel})$ denotes the phase space coordinates, and we calculated (22) using *Mathematica*.

A. Dynamics on the fringe

Once the particles have been initialized along the hard edge, we use the location z along the length of the Cartesian dipole as the independent variable describing particle dynamics. The positions in phase space consist of the transverse coordinates $\mathbf{x} = (x, y)$ and negative path length $\ell = -vt$, whose conjugate canonical momenta we defined to be \mathbf{P} and P_{\parallel} , respectively. The Hamiltonian governing motion in a static magnetic field is then

$$\mathcal{H} = -\sqrt{P_{\parallel}^2 - [\mathbf{P} - q\mathbf{A}(\mathbf{x}; z)]^2} - qA_z(\mathbf{x}; z), \quad (24)$$

where q is the particle charge and (\mathbf{A}, A_z) is the magnetic vector potential. Now, we define the dimensionless momenta by dividing by the reference value p_0 and subtracting off those of the nominal orbit as follows

$$p_x = P_x/p_0 - (1 + \delta) \sin \theta, \quad (25)$$

$$p_y = P_y/p_0, \quad (26)$$

$$\delta = P_{\parallel}/p_0 - 1. \quad (27)$$

The dynamics remains Hamiltonian with dimensionless $\mathcal{H} = \mathcal{H}/p_0$ if we retain the coordinates \mathbf{x} and introduce the (almost) path length difference $\tau = \ell + z + x \sin \theta$. While the subtraction of $\delta \sin \theta$ from the horizontal momentum may seem somewhat unusual, it ensures that $\mathbf{p} = \mathbf{0}$ when the transverse momenta at the magnet entrance vanish as shown by Eq. (15). Including the term $x \sin \theta$ for ℓ is required for the transformation to be canonical. Somewhat fortuitously, it also turns out that these coordinates simplify subsequent calculations.

Next, we introduce the dimensionless vector potential

$$(\mathbf{a}, a_z) = -\frac{q}{p_0} (\mathbf{A}, A_z), \quad (28)$$

where the sign convention is chosen such that $a_z \sim x/\rho$ for a dipole with bending radius ρ . We then choose a gauge where the vertical component $a_y = 0$, and assume that the transverse momenta and vector potential are small such that \mathbf{p}^2 and $a_x^2 \ll (1 + \delta)^2 \sec^2 \theta$. Under this assumption we expand the dimensionless Hamiltonian to arrive at

$$\begin{aligned} \mathcal{H}(\mathbf{x}, \mathbf{p}, \delta; z) &\approx \tan \theta (p_x + a_x) + a_z + \delta(1 - \cos \theta) \\ &+ \frac{\sec^3 \theta}{2(1 + \delta)} (p_x + a_x)^2 + \frac{\sec \theta}{2(1 + \delta)} p_y^2. \end{aligned} \quad (29)$$

In general the field is given by Eqs. (8) and (9), but the fringe field maps that interest us are obtained by taking the difference between the full motion and that of the hard edge model. In other words, the hard edge model defines the unperturbed Hamiltonian

$$\begin{aligned} \mathcal{H}_0(\mathbf{x}, \mathbf{p}, \delta; z) &= p_x \tan \theta + a_{z,0}(\mathbf{x}; z) + \delta(\cos \theta - 1) \\ &+ \frac{\sec^3 \theta}{2(1 + \delta)} p_x^2 + \frac{\sec \theta}{2(1 + \delta)} p_y^2, \end{aligned} \quad (30)$$

with the hard edge $a_{x,0} = 0$ and the unperturbed longitudinal vector potential

$$a_{z,0}(\mathbf{x}; z) = x \frac{q}{p_0} \Pi_1(z) + (x^2 - y^2) \frac{q}{p_0} \Pi_2(z) + (x^3 - 3xy^2) \frac{q}{p_0} \Pi_3(z). \quad (31)$$

Here, the hard edge field profiles are given by (10), (13), and (14), but our calculation will assume that we shift the origin of z such that $z_{\text{edge}} = 0$.

The unperturbed equations of motion are

$$\frac{dx}{dz} = \frac{\partial \mathcal{H}_0}{\partial p_x} = \tan \theta + \frac{\sec^3 \theta}{1 + \delta} p_x \quad (32)$$

$$\frac{dp_x}{dz} = -\frac{\partial \mathcal{H}_0}{\partial x} = -\frac{q\Pi_1}{p_0} - \frac{2q\Pi_2}{p_0} x - \frac{3q\Pi_3}{p_0} (x^2 - y^2) \quad (33)$$

$$\frac{dy}{dz} = \frac{\partial \mathcal{H}_0}{\partial p_y} = \frac{\sec \theta}{1 + \delta} p_y \quad (34)$$

$$\frac{dp_y}{dz} = -\frac{\partial \mathcal{H}_0}{\partial y} = \frac{2q\Pi_2}{p_0} y + \frac{6q\Pi_3}{p_0} xy. \quad (35)$$

These equations are exactly solvable only if there is no sextupole field in the body, $\Pi_3 = 0$. Fortunately, we are only interested in the particle motion in the vicinity of the fringe field, and so we need only write out the solution as a Taylor series in z . To the required order we have

$$x(z) \approx x_0 + z \tan \theta + \frac{z \sec^3 \theta}{1 + \delta} p_{x,0} - \frac{z^2 \sec^3 \theta q \Pi_1}{2(1 + \delta) p_0} - \frac{z^2 \sec^3 \theta q}{2(1 + \delta) p_0} [2\Pi_2 x_0 + 3\Pi_3 (x_0^2 - y_0^2)] \quad (36)$$

$$y(z) \approx y_0 + z \frac{\sec \theta}{1 + \delta} p_{y,0} + \frac{z^2 \sec \theta q}{2(1 + \delta) p_0} [2\Pi_2 y_0 + 9\Pi_3 x_0 y_0] \quad (37)$$

$$p_x(z) \approx p_{x,0} - z \frac{q}{p_0} [\Pi_1 + 2\Pi_2 x_0 + 3\Pi_3 (x_0^2 - y_0^2)] \quad (38)$$

$$p_y(z) \approx p_{y,0} + z \frac{q}{p_0} [2\Pi_2 y_0 + 9\Pi_3 x_0 y_0]. \quad (39)$$

Note that no derivatives of the hard edge envelopes arise, since such terms contribute $\sim z(d\Pi_j/dz) \propto \alpha z \delta(z) = 0$.

The perturbation Hamiltonian \mathcal{H}_1 includes a nonzero transverse vector potential \mathbf{a} in addition to corrections to the longitudinal a_z . In the electromagnetic gauge with zero vertical component the perturbation is described by

$$\mathcal{H}_1 = a_x(\mathbf{x}; z) \tan \theta + \frac{\sec^3 \theta}{(1 + \delta)^2} p_x a_x(\mathbf{x}; z) + \frac{\sec^3 \theta}{2(1 + \delta)^2} a_x^2(\mathbf{x}; z) + [a_z(\mathbf{x}; z) - a_{z,0}(\mathbf{x}; z)]. \quad (40)$$

We want a coordinate map at the magnet hard edge that approximately includes the effects of \mathcal{H}_1 , and we will develop such a map using Hamiltonian perturbation theory [14] in a manner similar to that of Ref. [3]. Our solution begins with the unperturbed Hamiltonian \mathcal{H}_0 and its associated dynamics Eqs. (36)–(39). We define \mathcal{B}_0 to be the map associated with the unperturbed dipole Hamiltonian \mathcal{H}_0 , and introduce the notation $\mathcal{B}_0(z|z_-)$ to describe the map from the location $z = z_-$ well outside the magnetic fringe field to the arbitrary position z . The map \mathcal{M} for the total Hamiltonian $\mathcal{H}_0 + \mathcal{H}_1$ can be written using the so-called reverse factorization (see, e.g., Ch. 10 of Ref. [14])

$$\mathcal{M} = \mathcal{B}_1(z|z_-) \mathcal{B}_0(z|z_-), \quad (41)$$

where \mathcal{B}_1 accounts for the perturbation \mathcal{H}_1 and satisfies the differential equation

$$\frac{d}{dz} \mathcal{B}_1 = -\mathcal{B}_1(\mathcal{B}_0 : \mathcal{H}_1 : \mathcal{B}_0^{-1}) = -\mathcal{B}_1 : \mathcal{H}_1^{\text{int}} :. \quad (42)$$

Here, we employ Dragt's colon notation for the Poisson bracket operator associated with the function f

$$:f: = \sum_{i=1}^3 \left(\frac{\partial f}{\partial q_i} \frac{\partial}{\partial p_i} - \frac{\partial f}{\partial p_i} \frac{\partial}{\partial q_i} \right), \quad (43)$$

and $\mathcal{H}_1^{\text{int}}$ is the interaction picture Hamiltonian.

The interaction picture Hamiltonian $\mathcal{H}_1^{\text{int}}$ is defined along the unperturbed trajectories, meaning that it also satisfies $\mathcal{H}_1^{\text{int}}(\mathcal{Z}; z) = \mathcal{H}_1(\mathcal{B}_0(z|z_-)\mathcal{Z}; z)$. Hence, $\mathcal{H}_1^{\text{int}}(z)$ depends upon the independent variable z from both its explicit z -dependence and through the evolution of the unperturbed particle motion.

As described previously and diagrammed in Fig. 3, the full fringe field map \mathcal{F} takes the particles that are initially at the hard magnet edge, propagates them to $z = z_-$ where the magnetic field is approximately constant, uses (41) to track the particles through the fringe fields, and then maps the particles back through the ideal magnetic field to the hard edge. This can be expressed by sandwiching the dipole field map \mathcal{M} from Eq. (41) between unperturbed dipole maps \mathcal{B}_0 to and from the edge as follows

$$\begin{aligned} \mathcal{F} &= \mathcal{B}_0(z_-|0) \mathcal{M} \mathcal{B}_0(0|z_+) \\ &= \mathcal{B}_0(z_-|0) [\mathcal{B}_1(z_+|z_-) \mathcal{B}_0(z_+|z_-)] \mathcal{B}_0(0|z_+) \\ &= \mathcal{B}_0(z_-|0) \mathcal{B}_1(z_+|z_-) \mathcal{B}_0(0|z_-). \end{aligned} \quad (44)$$

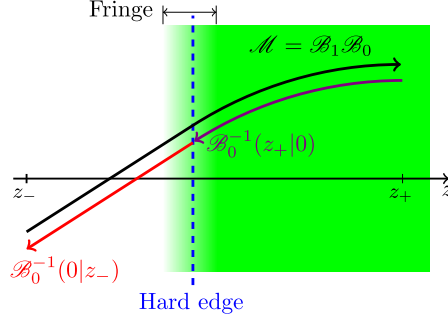


FIG. 3. Schematic of the fringe field map composite parts including the map to outside the fringe region (in red), through the fringe field (black), and back to the hard edge (violet).

Note that the ordering of the maps from left to right means that each one acts on the initial particle coordinates. To simplify Eq. (44) further, we write the field perturbation map through its exponential (Magnus) representation via $\mathcal{B}_1(z|z_-) = e^{:\mathcal{B}_1(z|z_-):}$. The generator of this map is given by the infinite series of Poisson brackets [14]

$$\begin{aligned} \mathcal{B}_1(z_+|z_-) &= - \int_{z_-}^{z_+} dz \mathcal{H}_1^{\text{int}}(z) \\ &+ \frac{1}{2} \int_{z_-}^{z_+} dz \int_{z_-}^z d\zeta : \mathcal{H}_1^{\text{int}}(\zeta) : \mathcal{H}_1^{\text{int}}(z) + \dots \end{aligned} \quad (45)$$

If we exponentiate this, insert into (44) and Taylor expand, the first order term is

$$\begin{aligned} \mathcal{B}_0(z_-|0) : \mathcal{H}_1^{\text{int}}(z) : \mathcal{B}_0(0|z_-) \\ &= \mathcal{B}_0(z_-|0) [\mathcal{B}_0(z|z_-) : \mathcal{H}_1(z) : \mathcal{B}_0^{-1}(z|z_-)] \mathcal{B}_0(0|z_-) \\ &= \mathcal{B}_0(z|0) : \mathcal{H}_1(z) : \mathcal{B}_0^{-1}(0|z) = : \mathcal{H}_1^{\text{int}}(z|0) :, \end{aligned} \quad (46)$$

where we have (temporarily) introduced the additional notation $\mathcal{H}_1^{\text{int}}(z|0)$ to emphasize that the interaction picture perturbation Hamiltonian at z is written in terms of initial coordinates at $z = 0$. The second order terms also reduce to ones that only involve $: \mathcal{H}_1(z|0) :$, as can be seen with the example

$$\begin{aligned} \mathcal{B}_0(z_-|0) : : \mathcal{H}_1^{\text{int}}(\zeta) : \mathcal{H}_1^{\text{int}}(z) : \mathcal{B}_0(0|z_-) \\ &= \mathcal{B}_0(\zeta|0) : : \mathcal{H}_1(\zeta) : \mathcal{B}_0^{-1}(\zeta|z_-) \mathcal{B}_0^{-1}(z_-|0) \\ &\quad \times \mathcal{B}_0(z_-|0) \mathcal{B}_0(z|z_-) \mathcal{H}_1(z) : \mathcal{B}_0^{-1}(z|0) \\ &= : : \mathcal{H}_1^{\text{int}}(\zeta|0) : \mathcal{H}_1^{\text{int}}(z|0) : . \end{aligned} \quad (47)$$

Here, we added the identity map $\mathcal{B}_0^{-1}(z_-|0) \mathcal{B}_0(z_-|0)$ between products of the interaction Hamiltonian to set \mathcal{H}^{int}

to be a function of the initial coordinates along the hard edge. Similar manipulations of higher order products should convince one that the fringe field map can therefore be written as

$$\mathcal{F} = e^{:\Omega_M:} \quad (48)$$

with Lie generator

$$\begin{aligned} \Omega_M &= - \int_{z_-}^{z_+} dz \mathcal{H}_1^{\text{int}}(z|0) \\ &+ \frac{1}{2} \int_{z_-}^{z_+} dz \int_{z_-}^z d\zeta : \mathcal{H}_1^{\text{int}}(\zeta|0) : \mathcal{H}_1^{\text{int}}(z|0) + \dots \end{aligned} \quad (49)$$

The mathematical gymnastics we used to arrive at (49) may have been somewhat opaque and perhaps suboptimal, but the physical meaning of the map (48) and its generator (49) should be clear: the Magnus (exponential) solution is given by an expansion in powers of an interaction Hamiltonian whose z -dependent coordinates are expressed in terms of the unperturbed values along the hard edge of the magnet. Hence, we evaluate (49) along the unperturbed trajectories (36)–(39), and all Poisson brackets are with respect to the “initial” coordinates $(x_0, y_0, p_{x,0}, p_{y,0})$ at the hard magnet edge.

B. Lie generator and resulting fringe field map for a Cartesian bend

We now have all the elements needed for our calculation. Before we go to our approximation of Ω_M , we first define the various fringe integrals that arise directly in terms of the generalized gradients $C_1(z)$, $C_2(z)$, and $C_3(z)$; note that these have dimensions of Tesla (T), T/m, and T/m², respectively. First, we recall that the nominal bending radii $1/\rho_{\pm}$ and focusing gradients K_{\pm} are defined in terms of the generalized gradients at z_{\pm} :

$$\frac{1}{\rho_{\pm}} = \frac{q}{p_0} C_1(z_{\pm}) \quad K_{\pm} = \frac{q}{p_0} 2C_2(z_{\pm}); \quad (50)$$

again, we set $C_i \rightarrow 0$ if the ideal region is vacuum. Next, recall that the hard edge is set such the integrated bending field in the hard edge model matches that of the actual dipole component:

$$\begin{aligned} \frac{q}{p_0} \int_{z_-}^{z_+} dz [C_1(z_+) \Theta(z - z_{\text{HE}}) + C_1(z_-) \Theta(z_{\text{HE}} - z)] \\ = \frac{z_+ - z_{\text{HE}}}{\rho_+} + \frac{z_{\text{HE}} - z_-}{\rho_-} = \frac{q}{p_0} \int_{z_-}^{z_+} dz C_1(z). \end{aligned} \quad (51)$$

Then, we define the following dipolar fringe field integrals:

$$\left(\frac{g^2 K_0}{\rho}\right) = \frac{q}{p_0} \int_{z_-}^{z_+} dz (z - z_{\text{edge}}) \{C_1(z_+) \Theta(z) + C_1(z_-) [1 - \Theta(z)] - C_1(z)\} \quad (52)$$

$$\left(\frac{gK_2}{\rho^2}\right) = \frac{q^2}{p_0^2} \int_{z_-}^{z_+} dz \{C_1(z) [C_1(z_+) + C_1(z_-) - C_1(z)] - C_1(z_+) C_1(z_-)\} \quad (53)$$

$$\left(\frac{K_3}{g\rho^2}\right) = \frac{q^2}{p_0^2} \int_{z_-}^{z_+} dz [C_1'(z)]^2. \quad (54)$$

The notation is lifted from Ref. [3], with g giving the magnetic gap so that K_0 , K_2 , and K_3 are dimensionless and give rise to terms that are $O(g^2)$, $O(g)$, and $O(1/g)$, respectively; the hard edge definition (51) ensures that the integral formerly known as K_1 vanishes. At the magnet entrance the fringe field integrals for electrons reduce to

$$\left(\frac{g^2 K_0}{\rho}\right) \rightarrow \frac{|e|}{p_0} \int_{z_-}^{z_+} dz (z - z_{\text{edge}}) [C_1(z) - C_1(z_+) \Theta(z)], \quad \left(\frac{gK_2}{\rho^2}\right) \rightarrow \frac{e^2}{p_0^2} \int_{z_-}^{z_+} dz C_1(z) [C_1(z_+) - C_1(z)],$$

and we find that K_2 as defined in (53) is a modest generalization of the usual field integration (FINT) parameter for vertical focusing from a dipole fringe field.

In addition, we will require the quadrupole fringe integrals

$$g^2 K I_1 = \frac{2q}{p_0} \int_{z_-}^{z_+} dz (z - z_{\text{edge}}) \{C_2(z) - C_2(z_+) \Theta(z) - C_2(z_-) [1 - \Theta(z)]\} \quad (55)$$

$$gK I_0 = \frac{2q}{p_0} \int_{z_-}^{z_+} dz \{C_2(z) - C_2(z_+) \Theta(z) - C_2(z_-) [1 - \Theta(z)]\}, \quad (56)$$

and the field curvature/sextupole integrals

$$\left(\frac{g^2 K_4}{R\rho}\right) = \frac{q}{p_0} \int_{z_-}^{z_+} dz (z - z_{\text{edge}})^2 \left\{6C_3(z) - \frac{1}{4} C_1''(z) - 6C_3(z_+) \Theta(z) - 6C_3(z_-) [1 - \Theta(z)]\right\} \quad (57)$$

$$\left(\frac{gK_5}{R\rho}\right) = \frac{q}{p_0} \int_{z_-}^{z_+} dz (z - z_{\text{edge}}) \left\{6C_3(z) - \frac{1}{4} C_1''(z) - 6C_3(z_+) \Theta(z) - 6C_3(z_-) [1 - \Theta(z)]\right\} \quad (58)$$

$$\left(\frac{K_6}{R\rho}\right) = \frac{q}{p_0} \int_{z_-}^{z_+} dz \left\{6C_3(z) - \frac{1}{4} C_1''(z) - 6C_3(z_+) \Theta(z) - 6C_3(z_-) [1 - \Theta(z)]\right\}. \quad (59)$$

The notation of (55) is adapted from the quadrupole calculations of Ref. [18] with their $(I_1^+ + I_1^-) = g^2 I_1$, while that of the field curvature terms (57)–(59) is again borrowed from [3] but now allow for body sextupole fields in the magnet. These last three integrals are due to the finite horizontal extent of the magnet, with R giving the field's radius of curvature. Finally, Eq. (56) represents a new fringe integral that quantifies the difference in the quadrupole fringe field profile from that of the dipole component. Note that if the magnet had no dipole component, we would define the quadrupole's hard edge by requiring the integral in (56) to vanish.

Having defined the fringe integrals, we are now in a position to write out the Lie generator of the fringe field map. The only remaining challenge is to choose what small parameters will be used to constrain the perturbation expansion. For example, since the distance that a particle travels in the fringe region scales with $g \sec \theta$, we should require both the gap g to be small and the angle θ to be not too large. We define the dimensionless small parameter ϵ , assume that the ordering satisfies $g/\rho \sim O(\epsilon)$ and $Kx^2 \sim p_x^2 \sim O(\epsilon^2)$, and retain terms in Ω_M through $O(\epsilon^3)$. In addition to this, we have found that contributions $\sim (gK_5/\rho)$ can sometimes be considerably larger

than other $O(\epsilon)$ terms, and so we will also keep this contribution at third order in the coordinates. The resulting Lie generator is then

$$\begin{aligned}\Omega_M = & \frac{\sec^3\theta}{2(1+\delta)} \left(\frac{g^2 K_0}{\rho} \right) p_x + \left[\frac{\tan^2\theta}{2} \left(\frac{g^2 K_4}{R\rho} \right) - \tan\theta \left(1 - \frac{1}{2} \tan^2\theta \right) (g^2 K I_1) \right] x \\ & + \left[- \left(\frac{\tan\theta}{\rho_+} - \frac{\tan\theta}{\rho_-} \right) + \frac{1 + \sin^2\theta}{\cos^3\theta(1+\delta)} \left(\frac{gK_2}{\rho^2} \right) + \left(1 + \frac{1}{2} \tan^2\theta \right) (gK I_0) \right] \frac{y^2}{2} \\ & + \tan\theta \left(\frac{gK_5}{R\rho} \right) \frac{y^2 \sec^2\theta - x^2}{2} - \left(1 - \frac{1}{2} \tan^2\theta \right) (gK I_0) \frac{x^2}{2} + \frac{\sec\theta}{1+\delta} (g^2 K I_1) (p_y y - p_x x) \\ & - \frac{\sec^2\theta}{1+\delta} \left(\frac{1}{\rho_+} - \frac{1}{\rho_-} \right) \frac{p_x y^2}{2} + \frac{\sec\theta}{1+\delta} \left(\frac{gK_5}{\rho R} \right) \left[p_y x y - p_x (x^2 - y^2) \frac{\sec^2\theta}{2} \right] \\ & - \frac{\tan\theta}{12} (K_+ - K_-) (3xy^2 + x^3) + \left(\frac{K_6}{R\rho} \right) \frac{3xy^2 \sec^2\theta - x^3}{6} - \frac{1 + \sin^2\theta}{\cos^3\theta(1+\delta)} \left(\frac{K_3}{g\rho^2} \right) \frac{y^4}{6}.\end{aligned}\quad (60)$$

The fringe field map can now be had by applying the exponentiated operator $e^{:\Omega_M:}$ to the coordinates at the hard edge. For example, the displacement due to the fringe fields in the horizontal direction is given by $\Delta x = (e^{:\Omega_M:} - 1)x$. At the end of this section we will express the full fringe field map as a sequence of symplectic coordinate updates, but to compare our results with previous work we first compute the Taylor map by expanding $e^{:\Omega_M:}$ to second order. The resulting corrections to the particle coordinates are then given by the sum of

$$\Delta x|_{\text{old}} = -\frac{\sec^3\theta}{1+\delta} \left(\frac{g^2 K_0}{\rho} \right) + \frac{\sec^3\theta}{2(1+\delta)} \left(\frac{1}{\rho_+} - \frac{1}{\rho_-} \right) y^2 \quad (61)$$

$$\Delta y|_{\text{old}} = 0 \quad (62)$$

$$\Delta p_x|_{\text{old}} = \frac{\tan^2\theta}{2} \left(\frac{g^2 K_4}{\rho R} \right) - \tan\theta \left(\frac{gK_5}{\rho R} \right) x + \left(\frac{K_6}{2\rho R} \right) \frac{y^2 - x^2 \cos^2\theta}{\cos^2\theta} \quad (63)$$

$$\begin{aligned}\Delta p_y|_{\text{old}} = & - \left(\frac{\tan\theta}{\rho_+} - \frac{\tan\theta}{\rho_-} \right) y + \frac{1 + \sin^2\theta}{(1+\delta)\cos^3\theta} \left(\frac{gK_2}{\rho^2} \right) y + \frac{\tan\theta}{\cos^2\theta} \left(\frac{gK_5}{\rho R} \right) y + \sec^2\theta \left(\frac{K_6}{\rho R} \right) xy \\ & - \frac{\sec^3\theta}{1+\delta} \left(\frac{1}{\rho_+} - \frac{1}{\rho_-} \right) y p_x + \frac{2\cos^2\theta - 4}{3(1+\delta)\cos^3\theta} \left(\frac{K_3}{\rho^2 g} \right) y^3\end{aligned}\quad (64)$$

and

$$\Delta x|_{\text{new}} = \frac{\sec\theta}{1+\delta} \left[(g^2 K I_1) x + \left(\frac{gK_5}{2\rho R} \right) \frac{x^2 - y^2}{\cos^2\theta} \right] \quad (65)$$

$$\Delta y|_{\text{new}} = -\frac{\sec\theta}{1+\delta} (g^2 K I_1) y - \frac{\sec\theta}{1+\delta} \left(\frac{gK_5}{\rho R} \right) xy \quad (66)$$

$$\begin{aligned}\Delta p_x|_{\text{new}} = & - \left(1 - \frac{1}{2} \tan^2\theta \right) (gK I_0) x - \frac{\sec\theta}{1+\delta} (g^2 K I_1) p_x - \frac{\tan\theta}{4} (K_+ - K_-) (x^2 + y^2) \\ & + \frac{\sec\theta}{1+\delta} \left(\frac{gK_5}{\rho R} \right) \left(p_y y - \frac{p_x x}{\cos^2\theta} \right) - \tan\theta \left(1 - \frac{1}{2} \tan^2\theta \right) (g^2 K I_1)\end{aligned}\quad (67)$$

$$\Delta p_y|_{\text{new}} = \left(1 + \frac{1}{2} \tan^2\theta \right) (gK I_0) x + \frac{\sec\theta}{1+\delta} (g^2 K I_1) p_y - \frac{\tan\theta}{2} (K_+ - K_-) xy + \frac{\sec\theta}{1+\delta} \left(\frac{gK_5}{\rho R} \right) \left(p_x x + \frac{p_y y}{\cos^2\theta} \right). \quad (68)$$

The Taylor map at a dipole entrance obtains by setting $\rho_+ = \rho$, $K_+ = K$, $\theta = \theta_{\text{entry}}$, and $K_- = 1/\rho_- = 0$. We show in Appendix B that in this case the ‘‘old’’ corrections (61)–(64) match those previously derived in [1–3], once the latter are

transported to the magnet hard edge. Similarly, the map at the dipole magnet exit has $\rho_- = \rho$, $K_- = K$, $\theta = -\theta_{\text{exit}}$, $K_+ = 1/\rho_+ = 0$, and the results of those same references can be reproduced by using the symmetries of the fringe integrals.

The “new” terms (65)–(68) include those associated with the quadrupole focusing and the formally third order contributions $\propto K_5$. We have found that the second order correction due to the hard edge quadrupole term does not match that of Brown; we believe that this is due to differing reference trajectories of the two. Regardless, in later

sections we will compare our predictions with particle tracking for an idealized magnet fringe profile.

Finally, we conclude this section with a symplectic implementation of the fringe map. There are several ways to “symplectify” a map, and in the Appendix we derive one scheme that uses the Lie generator to split the update into four separate steps. Each step is symplectic, and the composition is chosen such that the resulting map that agrees with (61)–(68) to our chosen order. Our update starts with the linear transformation

$$x_1 = x_0 e^b + X_d \frac{e^b - 1}{b} \quad (69)$$

$$y_1 = y_0 e^{-b} \quad (70)$$

$$p_{x,1} = p_{x,0} e^{-b} + P_d \frac{e^b - 1}{b e^b} - \left[\tan \theta \left(\frac{gK_5}{\rho R} \right) + \left(1 - \frac{1}{2} \tan^2 \theta \right) (gKI_0) \right] \left(\frac{\cosh b - 1}{b^2} X_d + \frac{\sinh b}{b} x_0 \right) \quad (71)$$

$$p_{y,1} = p_{y,0} e^b + \frac{\sinh b}{b} \left[\frac{1 + \sin^2 \theta}{\cos^3 \theta (1 + \delta)} \left(\frac{gK_2}{\rho^2} \right) - \left(\frac{\tan \theta}{\rho_+} - \frac{\tan \theta}{\rho_-} \right) + \frac{\tan \theta}{\cos^2 \theta} \left(\frac{gK_5}{\rho R} \right) + \left(1 + \frac{1}{2} \tan^2 \theta \right) (gKI_0) \right] y_0 \quad (72)$$

where X_d is the lowest-order horizontal offset due to the fringe, P_d is the displacement in p_x , and b effectively sets the magnification in each plane; these parameters are given by

$$b = \frac{\sec \theta}{1 + \delta} (g^2 KI_1), \quad X_d = -\frac{\sec \theta}{1 + \delta} \left(\frac{g^2 K_0}{\rho} \right),$$

$$P_d = \frac{\tan^2 \theta}{2} \left(\frac{g^2 K_4}{R\rho} \right) - \tan \theta \left(1 - \frac{1}{2} \tan^2 \theta \right) (g^2 KI_1). \quad (73)$$

After the linear map, we proceed with the nonlinear contributions

$$x_2 = x_1 \quad (74)$$

$$y_2 = y_1 \exp \left[-\frac{\sec \theta}{1 + \delta} \left(\frac{gK_5}{\rho R} \right) x_1 \right] \quad (75)$$

$$p_{x,2} = p_{x,1} + \frac{\sec \theta}{1 + \delta} \left(\frac{gK_5}{\rho R} \right) p_{y,1} y_1$$

$$- \left[\left(\frac{K_6}{\rho R} \right) + \tan \theta \frac{K_+ - K_-}{2} \right] \frac{x_1^2}{2} \quad (76)$$

$$p_{y,2} = p_{y,1} \exp \left[\frac{\sec \theta}{1 + \delta} \left(\frac{gK_5}{\rho R} \right) x_1 \right], \quad (77)$$

and then

$$x_3 = x_2 - \frac{\sec^3 \theta}{1 + \delta} \left[\left(\frac{gK_5}{\rho R} \right) - \left(\frac{1}{\rho_+} - \frac{1}{\rho_-} \right) \right] \frac{y_2^2}{2} \quad (78)$$

$$y_3 = y_2 \quad (79)$$

$$p_{x,3} = p_{x,2} + \left[\sec^2 \theta \left(\frac{K_6}{\rho R} \right) - \tan \theta \frac{K_+ - K_-}{2} \right] \frac{y_2^2}{2} \quad (80)$$

$$p_{y,3} = p_{y,2} + \frac{\sec^3 \theta}{1 + \delta} \left[\left(\frac{gK_5}{\rho R} \right) - \left(\frac{1}{\rho_+} - \frac{1}{\rho_-} \right) \right] p_{x,2} y_2$$

$$+ \left[\sec^2 \theta \left(\frac{K_6}{\rho R} \right) - \tan \theta \frac{K_+ - K_-}{2} \right] x_2 y_2, \quad (81)$$

and finally

$$x_4 = \left[1 - \frac{\sec^3 \theta}{1 + \delta} \left(\frac{gK_5}{\rho R} \right) \frac{x_3}{2} \right]^{-1} x_3 \quad (82)$$

$$y_4 = y_3 \quad (83)$$

$$p_{x,4} = \left[1 - \frac{\sec^3 \theta}{1 + \delta} \left(\frac{gK_5}{\rho R} \right) \frac{x_3}{2} \right]^2 p_{x,3} \quad (84)$$

$$p_{y,4} = p_{y,3} + \frac{2\cos^2 \theta - 4}{3\cos^3 \theta (1 + \delta)} \left(\frac{K_3}{\rho^2 g} \right) y_3^3. \quad (85)$$

We provide a derivation of the symplectic fringe field map (69)–(85) in the Appendix, and additionally include

the updates to the (negative) path length coordinate ℓ . This map has been incorporated into ELEGANT's Cartesian bending magnet element CCBEND, and we will discuss this and its predictions further in Sec. V. But first, we will verify our new fringe map predictions that were summarized by Eqs. (65)–(68).

IV. NUMERICAL TESTS

This section will compare our theoretical predictions for the fringe field maps with tracking results in several different scenarios. Within this section the tracking predictions are obtained using a custom code that numerically integrates the equations of motion that we will describe more fully later. In part A we isolate the “new” contributions proportional to the dipole focusing K , and verify their form using a simple, Enge-type model for the magnetic fringe field. Part B then compares the full fringe field theory using magnetic field models of gradient dipoles that are being built for the APS-U.

A. Tracking through idealized dipole fringe fields

This section will compare the fringe field corrections that come from the quadrupole focusing terms in Eqs. (65)–(68). We do this by comparing the theory to tracking using a fringe field that is described by the simplest, one-parameter Enge function [19], wherein longitudinal variation of the field at $x = y = 0$ is given by the logistic equation $1/(1 + e^{-z/g})$. In this case we can model the magnetic field using the exact expressions provided in Ref. [20], although a Taylor series description gives similar results. The dipole contribution is given by

$$B_y = \frac{p_0}{q\rho} \frac{1 + e^{-z/g} \cos(y/g)}{1 + 2e^{-z/g} \cos(y/g) + e^{-2z/g}} \quad (86)$$

$$B_z = \frac{p_0}{q\rho} \frac{e^{-z/g} \sin(y/g)}{1 + 2e^{-z/g} \cos(y/g) + e^{-2z/g}}, \quad (87)$$

while we model the quadrupole component using the symmetrized, one-parameter limit provided by Ref. [20] at the end of Sec. IV B:

$$B_x = \frac{p_0 K}{4q} \left[3 + \frac{\sinh(z/g)}{\cosh(z/g) + \cos(x/g)} \right] y - \frac{p_0 K}{2q} \operatorname{atan} \left[\frac{\sin(y/g)}{e^{z/g} + \cos(y/g)} \right] g \quad (88)$$

$$B_y = \frac{p_0 K}{4q} \left[3 + \frac{\sinh(z/g)}{\cosh(z/g) + \cos(y/g)} \right] x - \frac{p_0 K}{2q} \operatorname{atan} \left[\frac{\sin(x/g)}{e^{z/g} + \cos(x/g)} \right] g \quad (89)$$

$$B_z = \frac{p_0 K}{4q} \frac{\sin(y/g)}{\cosh(z/g) + \cos(y/g)} x + \frac{p_0 K}{4q} \frac{\sin(x/g)}{\cosh(z/g) + \cos(x/g)} y. \quad (90)$$

Our custom tracking code numerically evaluates the fringe field map using the following five steps: (1) Initialize coordinates on the hard edge $z = 0$. (2) Drift particles to $z = -10g$ where $\mathbf{B} \approx \mathbf{0}$. (3) Track particles through magnetic field (86)–(90) to $z = 10g$ where it is approximately constant. (4) Back-track the particles to $z = 0$ using the ideal field $\mathbf{B} = (p_0/q)(1/\rho + Ky, Kx, 0)$. (5) Compute coordinate differences at hard edge.

The tracking comparisons aim to verify the theory over a wide range of magnet parameters and initial conditions. To this end, our results include initial angles in the range $|\theta| \leq \pi/16$, focusing gradients $|K| \leq 4 \text{ m}^{-2}$, and magnetic gaps such that $50 \text{ mm} \geq g \geq 5 \text{ mm}$. The tracking presented here also assumes that $\rho = 20 \text{ m}$, but we have found similar results for bending radii larger than 5 m. Finally, we choose initial coordinates with $|x_0|, |y_0| \leq g/2$, similar ranges for $p_{x,0}$ and $p_{y,0}$, and energies with $|\delta| \leq 20\%$.

We begin our comparison by summarizing in Fig. 4 the tracking results for the “new” linear corrections $\propto (g^2 KI_1)$ from Eqs. (65)–(68). Specifically, these terms are given by

$$(\Delta x, \Delta p_x) = \frac{1 - \frac{3}{2} \tan^2 \theta}{1 + \delta} (g^2 KI_1) (-x_0, p_{x,0}) \quad (91)$$

$$(\Delta y, \Delta p_y) = \frac{1 + \frac{1}{2} \tan^2 \theta}{1 + \delta} (g^2 KI_1) (y_0, -p_{y,0}), \quad (92)$$

where for the Enge field $I_1 = \pi^2/6$. Panel (a) plots horizontal tracking results, where the plotted Δx subtracts off the zeroth-order orbit error $x_{\text{orbit}} = (g^2 K_0/\rho) \sec^3 \theta / (1 + \delta)$, while the plotted Δp_x subtracts off the theoretical orbit angle $p_{x,\text{orbit}} = \tan \theta (1 - \frac{1}{2} \tan^2 \theta) (g^2 KI_1)$ (green). The scaling is chosen such that the theory predicts a straight line with slope -1 ($+1$) for Δx (Δp_x). This trend is closely followed for Δx in red, but we can observe some deviations for Δp_x in green. We have found that the difference can be largely attributed to small deviations from the theoretical orbit angle offset; if we instead subtract off the numerically determined $p_{x,\text{orbit}}^{\text{sim}}$, then we get the blue points that are in very good agreement with expectations. Although the next-order correction to $p_{x,\text{orbit}}$ is calculable in principle, for all the parameters tested it constitutes a less than 6% correction to $p_{x,\text{orbit}}^{\text{theory}}$ that does not appear to be worth the trouble.

A similar graph for the vertical coordinates is shown in Fig. 4(b), but in this case there is no orbit deviation. With the chosen scaling the points for Δy should theoretically lie on a line with unit slope, while those for Δp_y are predicted to have a slope of -1 .

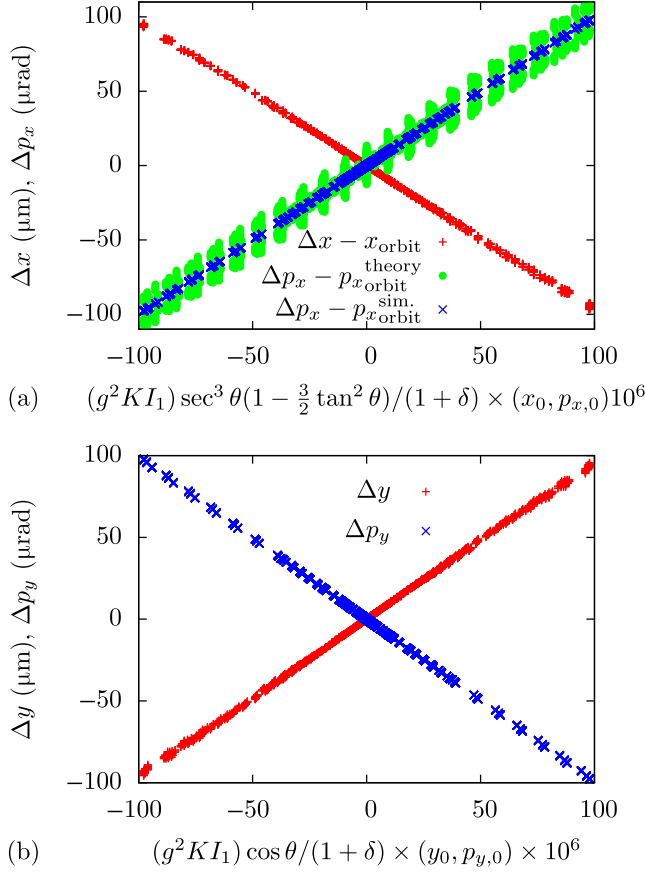


FIG. 4. Tracking results for the corrections of Eqs. (91) and (92). (a) Plots the observed Δx and Δp_x as a function of the scaled initial x_0 and $p_{x,0}$, scaled such that the theory predicts lines with slopes equal to ∓ 1 . The green points remove the theoretical orbit error $p_{x,\text{orbit}} \propto g^2$, while the blue removes the orbit angle observed in the simulations. (b) Plots the same results for the vertical plane, where theory predicts slopes for Δy and Δp_y equal to ± 1 .

Our next comparison concerns the second order corrections to p_x and p_y due to the focusing. In this case the theory predicts $\Delta p_x = -(K/4) \tan \theta (x_0^2 + y_0^2)$ and $\Delta p_y = -(K/2) \tan \theta (x_0 y_0)$. We tested these nonlinear corrections to the momenta by varying both coordinates x_0 and y_0 . We summarize the resulting tracking predictions in Fig. 5.

The red points in Fig. 5(a) plot the tracking results for Δp_x as a function of the scaled magnitude of the particle offset once we have subtracted off the zeroth-order offset $p_{x,\text{orbit}}$. The scaling is chosen such that the theory predicts the points to lie on the parabolas $y = \pm x^2$, and while this general trend is followed, there are some significant deviations. We found empirically that these discrepancies can be attributed to a focusing term that is third order in the gap. If we subtract off this small focusing correction $\propto g^3 K^2 x_0$ we obtain the blue points, which lie neatly along the theoretical prediction. This higher-order fringe focusing

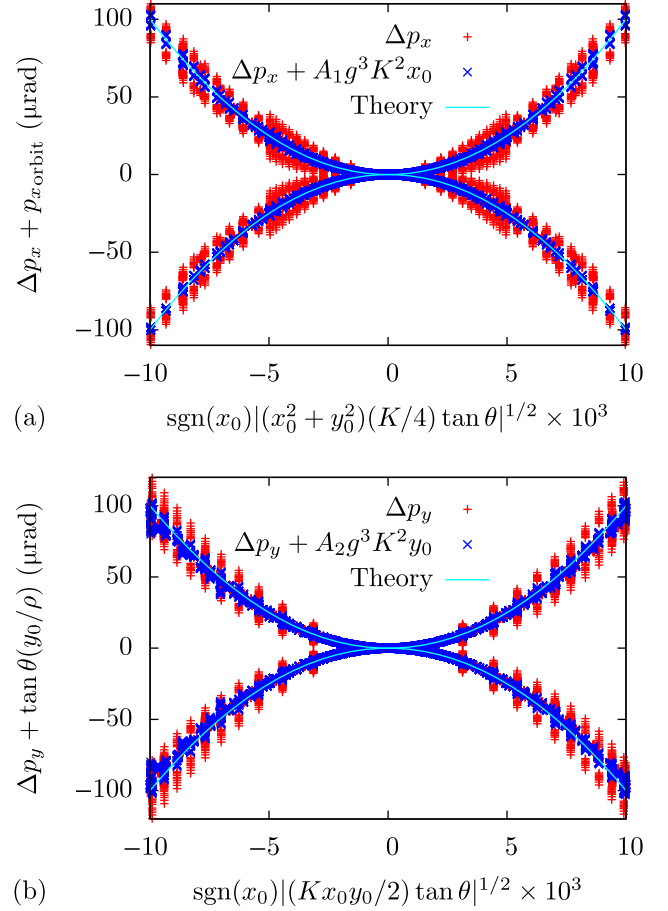


FIG. 5. Tracking results for the second-order focusing corrections. (a) Plots the observed Δp_x corrected by the zeroth order $p_{x,\text{orbit}}$ as a function of the scaled magnitude of the particle offset; the scaling is chosen such that the points should fall on the parabolas $y = \pm x^2$ shown in cyan. The red points indicate this trend, while the blue correct for an empirically determined linear focusing term $\propto g^3 K^2 x_0$. (b) Plots the observed Δp_y corrected by the theoretical focusing as a function of $|x_0 y_0|^{1/2}$ scaled such that the theory follow $y = \pm x^2$. The red points show this trend, which becomes even clearer if we also subtract off an empirically determined linear focusing term $\propto g^3 K^2 y_0$.

appears relevant here because the idealized field (86)–(90) assumes that the dipole and quadrupole components have identical field profiles, meaning that the fringe integral $I_0 = 0$. In the more realistic gradient dipoles that we have studied the focusing is dominated by Eq. (67)'s correction $\sim (g K I_0) x_0$, in which case the third order focusing term can be neglected.

Figure 5(b) plots analogous tracking results for Δp_y as a function of the scaled offset product $|x_0 y_0|^{1/2}$, once the theoretical linear focusing terms has been subtracted off. The scaling for the independent variable is again such that the points should theoretically lie along the parabolas $y = \pm x^2$. The red points generally follow this trend, with evidence of similar differences to that observed in panel (a).

If we again subtract off an empirically determined focusing $\propto g^3 K^2 y_0$ we obtain the blue points, which again show that the nonlinear corrections are well described by the theory. Again, the empirical focusing is typically a small correction to the term $\sim (gKI_0)y_0$ for realistic gradient dipoles, and is also smaller than the hard-edge focusing term we subtracted off.

We conclude this section by providing tracking results for a simplified longitudinal gradient dipole. For this we set the focusing gradient $K = 0$, and choose a bending field that smoothly transitions between two values by replacing $1/\rho \rightarrow (1/\rho_+ - 1/\rho_-)$ in the bending field (86) and (87) and then adding the constant field $p_0/q\rho_-$ to B_y . We track particles using the same procedure described previously, except that in Step 2 we transport particles from the hard edge to $z = -10g$ assuming a constant bending field $B_y = p_0/q\rho_-$. In addition, we will fix $\rho_- = 10$ m, vary ρ_+ between 15 and 100 m, and otherwise use the same range of initial conditions, angles, energies, and magnetic gaps as was done previously.

We summarize the tracking results for the vertical focusing in Fig. 6(a), for which we have subtracted off the dominant term $\tan\theta(1/\rho_+ - 1/\rho_-)y_0$, whose size for our parameters is typically between 10 and 400 μrad . The red points plot the resulting displacement versus the soft fringe focusing term

$$\frac{1 + \sin^2\theta}{\cos^3\theta(1 + \delta)} \left(\frac{gK_2}{\rho^2} \right) y_0 = \frac{1 + \sin^2\theta}{\cos^3\theta} \frac{g(\rho_+ - \rho_-)^2}{(1 + \delta)\rho_+^2\rho_-^2} y_0,$$

so that the theory predicts the points should lie along the line with unit slope. Figure 6(a) verifies the linear trend with some outliers. We found that these largely correlated to small magnetic gaps, and after subtracting off the pseudo-octupole correction $\propto y_0^3/g$ given by the final term in (64) and derived previously in [2,3], we find the very good agreement shown by the blue points.

Our next test targets the hard-edge, second-order contributions to Δx and Δp_y that are given by

$$\Delta x = \frac{\sec^3\theta}{2(1 + \delta)} \left(\frac{1}{\rho_+} - \frac{1}{\rho_-} \right) y_0^2$$

$$\Delta p_y = -\frac{\sec^3\theta}{(1 + \delta)} \left(\frac{1}{\rho_+} - \frac{1}{\rho_-} \right) y_0 p_{x,0}.$$

To isolate these terms we set $\theta = 0$ and plot the tracking output as a function of $|(1/\rho_+) - 1/\rho_-|/(1 + \delta)|^{1/2}y_0$ in Fig. 6(b). The red points plot the horizontal displacement from the orbit offset $\Delta x - x_{\text{orbit}}$, which lie closely along the theoretical line $-x^2/2$. The dark blue and black points plot the vertical momenta after we subtract off the linear soft fringe focusing for $y_0 = p_{y,0}$ and $y_0 = -p_{y,0}$, respectively. The tracking is clustered about the theoretical lines $y = \pm x^2$ as predicted.

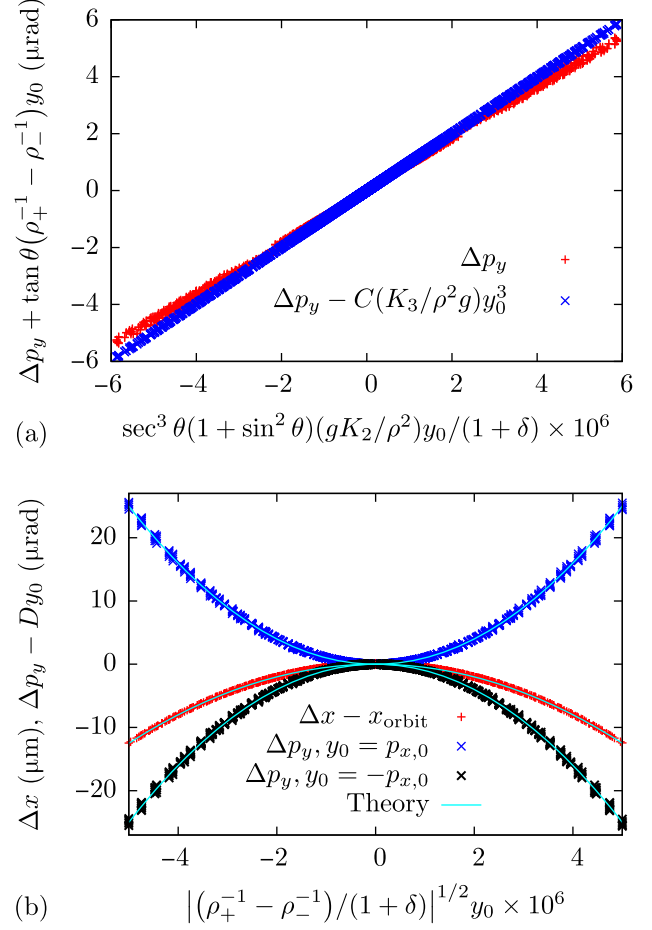


FIG. 6. (a) Vertical focusing for a longitudinal gradient dipole as a function of the soft fringe size after subtracting off the dominant term $\propto \tan\theta(1/\rho_+ - 1/\rho_-)$ (red). Theory predicts a unit slope. The blue points also subtract off the cubic correction $\propto y_0^3/g$. (b) Quadratic fringe terms for Δx and Δp_y for $\theta = 0$ as a function of the scaled $y_0 = \pm p_{y,0}$. Cyan theory lines are $y = x^2/2$ for the red points and $y = \pm x^2$ for blue and black points.

B. Fringe field tracking through APS-U dipoles

The APS-U will employ several Cartesian dipoles [21] whose parameters we summarize in Table I. The Q4 and Q5 magnets are reverse bends with strong focusing gradients, while the A:M1 magnet varies the bending field

TABLE I. Cartesian dipole parameters in the APS-U.

Magnet	Length (m)	ρ (m)	K (1/m ²)
Q4	0.211	-126.6	4.00
Q5	0.104	-89.8	2.16
A:M1.1	0.154	27.5	-8×10^{-4}
A:M1.2	0.179	43.7	-5×10^{-4}
A:M1.3	0.370	65.4	-3×10^{-4}
A:M1.4	0.543	87.1	-3×10^{-4}
A:M1.5	0.910	130.6	-2×10^{-4}

longitudinally using five magnetic segments as indicated; the APS-U also has a B:M1 magnet that is related to the A:M1 by mirror symmetry along z . This section compares our theoretical fringe map predictions to those obtained from tracking through the Q4 and A:M1 magnets. The tracking results are again obtained from our custom code essentially following the five steps described in the previous subsection. Here, however, the drift in step 2 goes to the beginning of the field map, while the particle integration of step 3 proceeds to a location z_+ in the middle of the magnetic segment. Unlike the previous test cases, we have found that the soft fringe corrections for the Q4 and A:M1 magnets are dominated by the dipole field curvature terms $\propto K_4, K_5$, and K_6 .

First, we compare the theoretical fringe field corrections with those obtained by tracking for the Q4 reverse gradient bend. We summarize our predictions for the coordinate maps as a function the initial coordinate offsets $x_0 = y_0$ in Fig. 7. We find excellent agreement between predictions

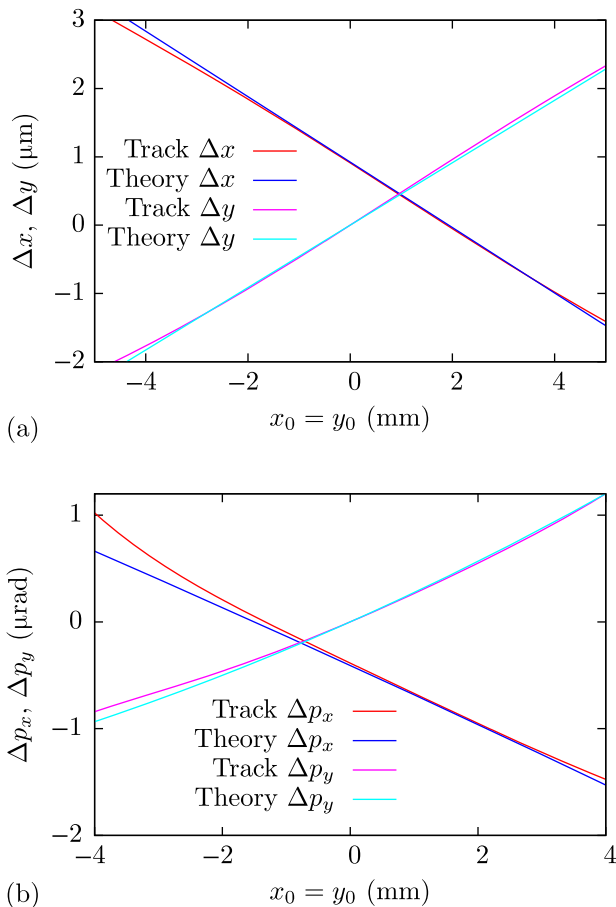


FIG. 7. Comparison of the fringe theory to tracking for the Q4 reverse bend dipole. (a) Compares the offsets Δx and Δy as a function of initial $x_0 = y_0$, while (b) plots the angles Δp_x and Δp_y . The “old” theory predicts a nearly constant $\Delta x|_{\text{old}} \approx 0.92 \mu\text{m}$, $\Delta p_x|_{\text{old}} \approx -0.41 \mu\text{rad}$, and $\Delta y|_{\text{old}} = \Delta p_y|_{\text{old}} = 0$ due to the large bending radius $\rho = -126.6 \text{ m}$.

and theory provided $|x_0| \sim |y_0| \lesssim 2 \text{ mm}$, after which higher order nonlinearities lead to larger discrepancies, particularly for the momenta. We have found similarly good agreement when the initial coordinates are less than a few mm or mrad for other fringe corrections.

Next, we will compare our fringe predictions to those obtained from tracking through the A:M1 longitudinal gradient dipole. Figure 8(a) shows how the bending field varies longitudinally in five discrete segments, with the black line showing the reference orbit. In addition, the black dots indicate the theoretically obtained locations of the six hard edges. At each of those locations we repeat the five steps of fringe field tracking that we described in the previous section, meaning that we have six different fringe field maps for the A:M1 magnet.

We compare the tracking results to theoretical predictions for the change in the horizontal momentum as a function of the initial horizontal offset x_0 in Fig. 8(b), wherein we offset the data by the fringe number $0 \leq f \leq 5$ for clarity. We see that each line is horizontally centered about the reference orbit, and each contains both first and second order contributions. Figure 8(c) plots Δp_x as a function of the vertical y_0 , and we find that the nearly quadratic theoretical predictions agrees well with tracking each fringe location over the entire range of coordinates investigated.

Figure 9 plots the fringe offsets for the vertical momentum. Panel (a) plots the focusing Δp_y as a function of vertical y_0 assuming all other coordinates vanish. Both tracking and theory show that the vertical fringe focusing goes from positive to negative as the particle traverses the magnet. It turns out that the dominant contribution to this trend comes from the nonzero orbit via the curvature term $\propto [(K_6/\rho R)x_{\text{ref}}]y_0$; this term more than cancels the oppositely signed hard edge correction $\tan\theta(y_0/\rho_- - y_0/\rho_+)$, and the only other significant contribution comes from the soft-fringe fringe focusing $\propto (gK_2/\rho^2)y_0$.

Finally, Fig. 9(b) plots Δp_y when we set the vertical displacement y_0 equal to the horizontal offset from the reference orbit $x_0 - x_{\text{ref}}$. We see that in addition to the linear contributions seen in panel (a), we also have important quadratic dependence from the term $\propto (K_6/\rho R)(x_0 - x_{\text{ref}})y_0$. For this magnet the terms involving the quadrupole gradient K are all close to zero.

V. CARTESIAN BENDS FOR TRACKING: THE CCBEND AND LGBEND ELEMENTS IN ELEGANT

Thus far we have discussed fringe field modeling in straight dipoles, with particular emphasis on the theory of Cartesian dipoles whose bending fields incorporate transverse or longitudinal gradients. The tracking code ELEGANT models Cartesian dipoles with no longitudinal gradient using the CCBEND element, while steplike longitudinal variations in the bending field are simulated using the

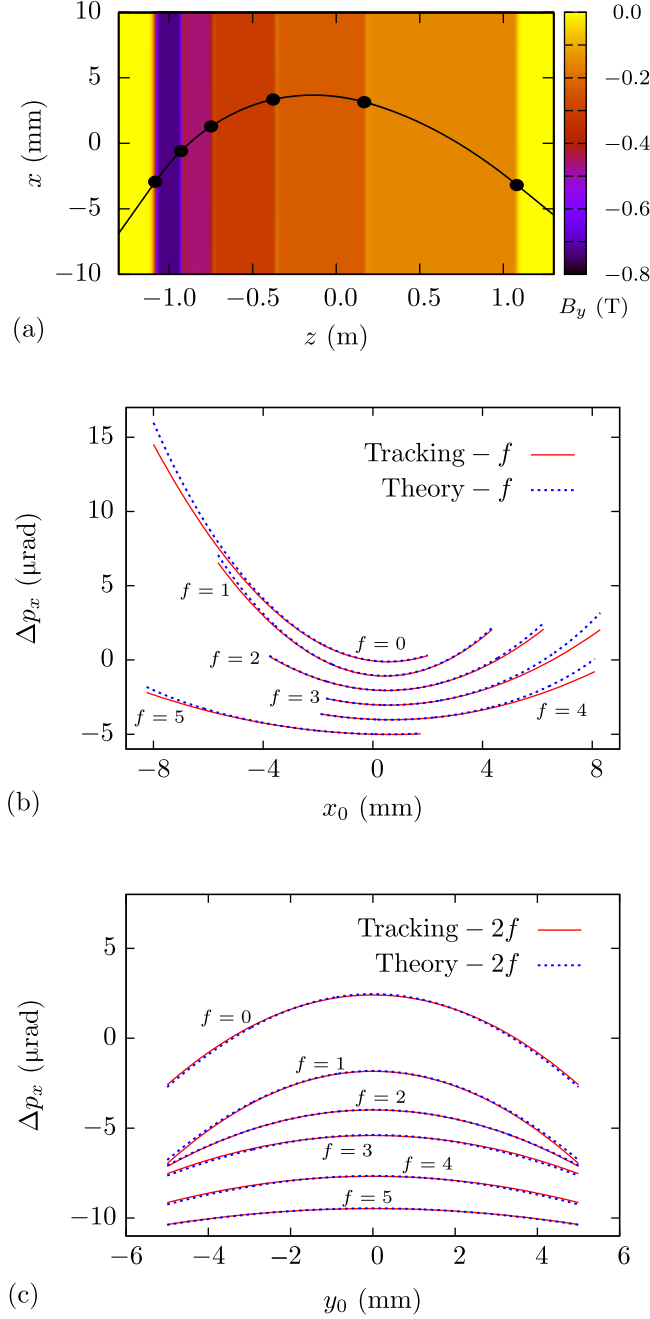


FIG. 8. (a) The A:M1 longitudinal gradient dipole field profile and reference orbit, where the hard edge locations of each magnetic segment are identified with the black points. (b) Comparison of tracking (red solid lines) with theory (blue dashed lines) for the fringe field corrections Δp_x as a function of input x_0 at each hard edge. The lines are displaced by the fringe number $0 \leq f \leq 5$ for clarity. (c) Analogous comparisons of tracking and theory for the approximately quadratic Δp_x as a function of vertical coordinate y_0 at each edge.

LGBEND element. In this section we describe how the fringe field maps were incorporated into these elements, and show examples of what these models predict for the APS-U lattice.

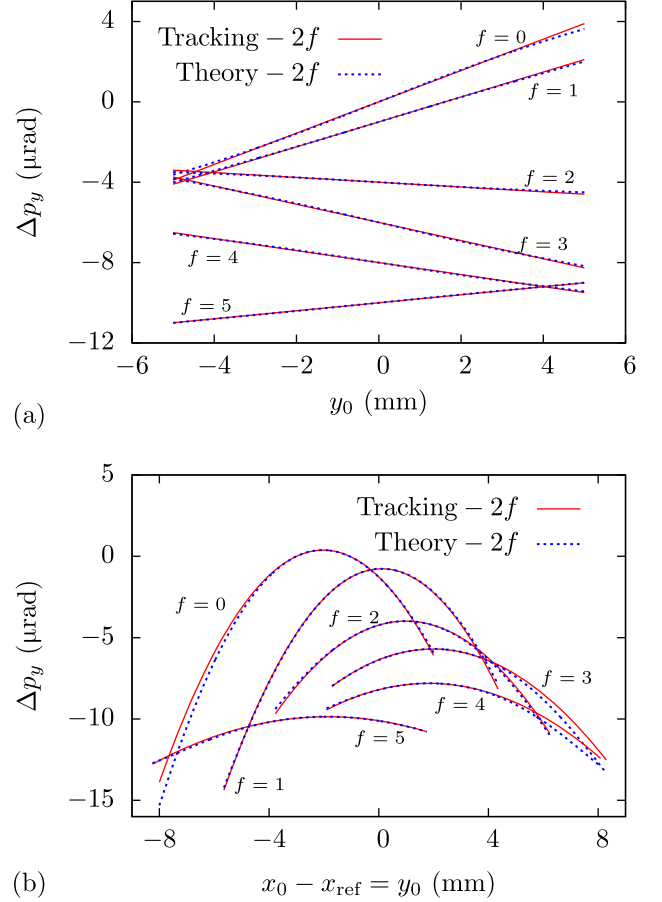


FIG. 9. (a) Vertical fringe field focusing for the APS-U longitudinal gradient dipole. The tracking is plotted in red while the theory is blue and dashed, and each prediction has been offset by twice the fringe number for clarity. (b) Linear and nonlinear fringe field corrections Δp_y for initial coordinates such that $x_0 = y_0 + x_{\text{ref}}$.

A. Tracking through Cartesian bends in ELEGANT

We begin by briefly describing how ELEGANT models Cartesian bends [22]. The first step is to transform the particle coordinates from the entrance plane to the hard edge as given in Eqs. (15)–(21). Then, the exact Hamiltonian of a hard-edge magnet in Cartesian coordinates is

$$\mathcal{H}(\mathbf{x}, \mathbf{p}, \delta) = -\sqrt{(1 + \delta)^2 - p_x^2 - p_y^2} + a_z(x, y), \quad (93)$$

where the longitudinal vector potential a_z describes the magnet's multipole content such that the usual dipole contribution is linear in x . We symplectically integrate the particle trajectories associated with (93) using the usual splitting (kick-drift) technique. Since the exact Hamiltonian is used, the need to use a curvilinear coordinate system is obviated. In this algorithm the numerical solution is obtained by interleaving exact solutions of the kinetic

square root term (the drift) with that of the potential a_z (the kick) as described in Refs. [23,24]; we typically use the fourth order scheme first introduced by Ruth [25], but a sixth order integrator is also available.

While the particle tracking just described is similar to that in other straight magnets, in dipoles one must take particular care to preserve the reference trajectory. For example, discretization errors in Cartesian bends can lead to unphysical changes of the reference orbit that are not present in sector bends, since the latter has a reference trajectory at $x = 0$. Even if numerical errors are minimized, multipole components effectively change the bending field as the particle moves off-axis, so that combined-function or nonideal magnets must account for a varying bending field along the trajectory. We have chosen to preserve the reference trajectory and to center it about $x = 0$ within the CCBEND element by adjusting both its field strength and its horizontal position. This is done by tracking the reference trajectory from the entrance hard edge at $z = 0$ to the exit hard edge at $z = L$, and applying a simplex optimization of the fractional strength error and horizontal offset that targets $x(0) = x(L)$, $p_x(0) = -p_x(L)$, and the initial and maximum x to have equal magnitudes but opposite signs. The first two conditions ensure that the reference trajectory starts and ends with the correct coordinates, while the third condition centers the orbit in the magnet to make best use of the good field region.

The symplectic fringe field maps (69)–(85) are applied at each edge. In addition, the CCBEND incorporates many of the ELEGANT’s “standard” capabilities, including reverse tracking, arbitrary misalignments, synchrotron radiation in particle tracking, interior apertures, and six-dimensional beam moment propagation with radiation damping and diffusion.

Tracking in the LGBEND element can be usefully thought of as tracking through a one full CCBEND element followed by a series of CCBENDs, each of which has their own exit plane position, angle, and fringe field map, but whose entrance plane position and angle is inherited from the prior segment. Hence, an LGBEND element with N magnetic segments requires $N + 1$ horizontal offsets, angles, and sets of fringe field integrals. The trajectory optimization, on the other hand, proceeds over the entire magnet, and with targets such that the entrance and exit horizontal positions and angles match those specified in the user-supplied configuration files.

Finally, the ELEGANT distribution provides the companion program `straightDipoleFringeCalc` to help define the Cartesian bend parameters and compute the fringe field integrals.

B. Application to the APS-U lattice

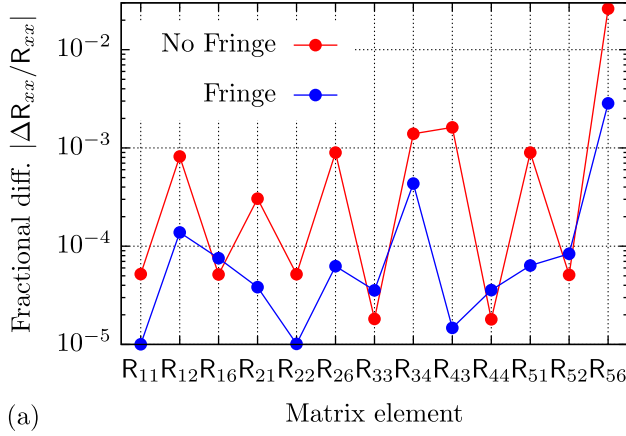
In this section we show how incorporating the fringe field terms into the CCBEND and LGBEND elements

impacts modeling of the APS-U lattice. In particular, we will compare predictions using full field tracking of the Q4, Q5, and A:M1 magnets listed in Table I to hard edge models that variously include or neglect the fringe field maps. The full-field tracking results are found by tracking with generalized gradients using the BGGEXP element [17] in ELEGANT. The generalized gradients themselves are derived from OPERA field maps of the magnets that are described in Ref. [21] using the tools described in Ref. [17]. We use numerical computation of first- and second-order transport matrices as the means of comparison, with the BGGEXP element taken as the “gold standard” against which more approximate, faster methods (i.e., CCBEND, LGBEND) are judged.

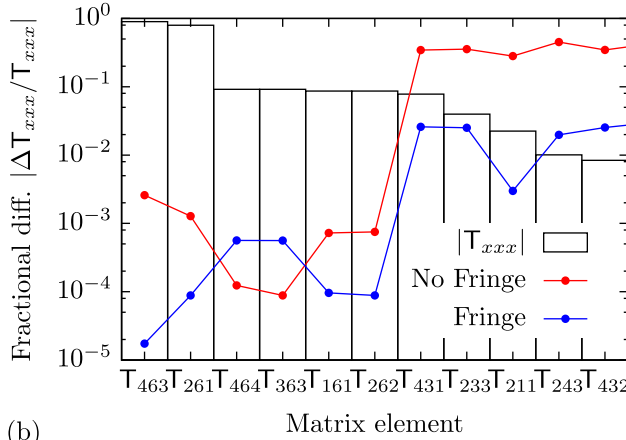
We begin with a detailed analysis of the Q4 reverse bend transverse gradient magnet, summarized in Fig. 10. Panel (a) compares the linear matrix elements by plotting the fractional difference between the full-field tracking with BGGEXP to those with (blue) and without (red) the fringe field contributions. We see that the predictions with the fringe field contributions typically agree to within a few parts in 10^4 or better, and that these usually improve agreement over those without the fringe maps by a factor of 5 to 10. Significantly, the model without the fringe maps predicts too much focusing in both planes, meaning that it cannot be corrected by adjusting K ; in other words, without fringe effects the absolute magnitude of both R_{21} and R_{43} is too large by the amount shown in Fig. 10, while the fringe map reduces this discrepancy largely by the “magnification” terms $(x, p_x) \rightarrow (e^b x, e^{-b} p_x)$ and $(y, p_y) \rightarrow (e^{-b} y, e^b p_y)$.

Figures 10(b) and 10(c) compares the nonzero second-order matrix elements that do not contribute to the path length, with the terms grouped from the largest in (a) to the smallest in (b). While the model without fringe contributions does well for the largest hard edge terms, once $T_{xxx} \lesssim 0.1$ we see errors as large 30%–40%. On the other hand, including the fringe contributions results in a fractional error of better than a few percent for all terms.

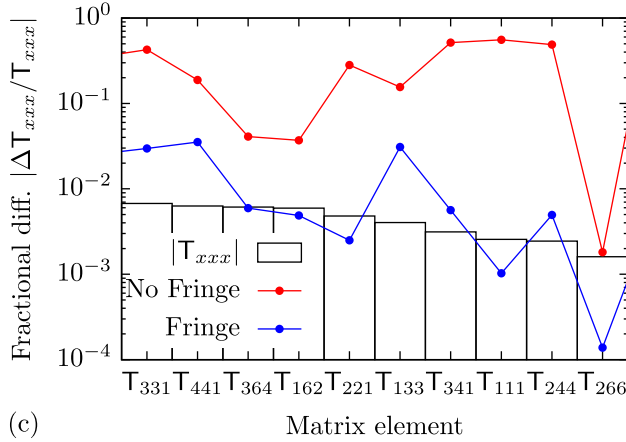
The differences in the matrix elements, although small, lead to noticeable differences in the linear lattice predictions for the APS-U. We summarize these in Table II, in which we list the linear tunes and chromaticities as obtained by tracking in the APS-U lattice for various models of the reverse bend gradient dipoles Q4 and Q5. We see that the fringe field terms change the tunes by 0.03–0.06, which is significant for a machine that plans to operate on the difference resonance. In addition, we see that neglecting the Q4 fringe maps leads to tunes that are too large in both planes, so that this cannot be fixed by adjusting the focusing strength. Note that the design APS-U tunes are 95.1 and 36.1, but that the lattice is not yet adjusted to compensate for improved models of Q4 or Q5.



(a)



(b)



(c)

FIG. 10. Fractional differences between the Q4 transverse gradient dipole matrix element predictions computed using BGGEXP magnet field tracking and CCBEND models that include (blue) and do not include (red) the fringe fields. (a) Plots the differences in the linear elements, while (b) and (c) plot the nonlinear elements as ranked from largest to smallest, and not including path length terms.

Next, we compare predictions for the longitudinal gradient A:M1 dipole. The linear matrix obtained from BGGEXP tracking through the full magnetic field is

TABLE II. APS-U lattice predictions for various models of the transverse gradient reverse bend dipoles, where (F) includes fringe maps while (NF) does not.

Model	ν_x	ν_y	Natural ξ_x	Natural ξ_y
(NF) CCBEND Q4	94.999	36.152	-131.79	-112.29
(F) CCBEND Q4	94.983	36.087	-131.41	-111.79
BGGEXP Q4	94.986	36.088	-131.45	-111.79
(NF) CCBEND Q5	95.136	36.069	-134.56	-111.07
(F) CCBEND Q5	95.115	36.076	-133.94	-111.39
BGGEXP Q5	95.116	36.076	-133.95	-111.39
(NF) CCBEND Q4+Q5	95.035	36.120	-132.65	-111.71
(F) CCBEND Q4+Q5	94.998	36.063	-131.68	-111.54
BGGEXP Q4+Q5	95.000	36.064	-132.05	-111.54

$$\begin{bmatrix} 0.99822 & 2.2243 & 0 & 0 & 0 & 0.04035 \\ -0.00101 & 0.9995 & 0 & 0 & 0 & 0.02857 \\ 0 & 0 & 1.0009 & 2.2251 & 0 & 0 \\ 0 & 0 & 0.00051 & 1.0002 & 0 & 0 \\ 0.02856 & 0.0232 & 0 & 0 & 1 & 0.00029 \\ 0 & 0 & 0 & 0 & 0 & 1 \end{bmatrix},$$

while that of the hard edge LGBEND is

$$\begin{bmatrix} 0.99816 & 2.2242 & 0 & 0 & 0 & 0.04029 \\ -0.00106 & 0.9995 & 0 & 0 & 0 & 0.02857 \\ 0 & 0 & 1.0010 & 2.2253 & 0 & 0 \\ 0 & 0 & 0.00056 & 1.0003 & 0 & 0 \\ 0.02856 & 0.0233 & 0 & 0 & 1 & 0.00029 \\ 0 & 0 & 0 & 0 & 0 & 1 \end{bmatrix}.$$

The agreement is quite good, such that the only element whose fractional difference is larger than 0.5% is the very small $R_{34} \sim 0.0005$. If we do not include the fringe field maps between the segments the agreement in the linear terms is only a little worse. On the other hand, neglecting the fringe field contributions results in very poor predictions for the second order terms; we have found that more than half of the terms differ by factors of two or more, with some having the same order of magnitude but the wrong sign.

We compare the second order matrix elements of the A:M1 longitudinal gradient dipole in Fig. 11, where we have ordered the elements according to the absolute value of their size and omitted the path length terms. The agreement is not as good as that observed for the single CCBEND magnet; the elements typically differ by 10%–25%, and differences approaching 100% can be observed for a few of the smaller elements in panel (b). Nevertheless, the hard edge LGBEND model provides a good representation for the APS-U lattice. We summarize the APS-U lattice

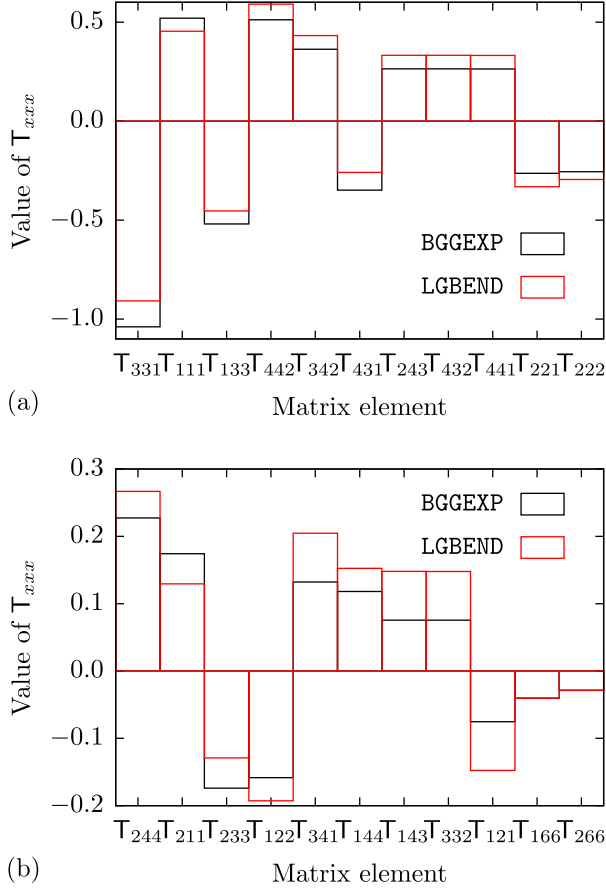


FIG. 11. Second order matrix element predictions for the A:M1 longitudinal gradient dipole as computed from BGGEXP magnet field tracking (black) and the LGBEND model (red). Panel (a) contains elements whose absolute value is greater than 0.4, while panel (b) the remaining ones.

predictions when we use various models for the M1 longitudinal gradient dipoles in Table III. Note that these include the respective models for both the A:M1 dipole listed in Table I and the B:M1 dipole that is related by mirror reflection along z (i.e., the B:M1 dipole starts with segment M1.5, followed M1.4, etc.).

As with the Q4 and Q5 examples, the effect of the improved longitudinal-gradient dipole models on the vertical tunes is operationally significant. Fortunately, the

TABLE III. APS-U lattice predictions for various models of the M1 longitudinal gradient bends.

Quantity	BGGEXP	(F) LGBEND	(NF) LGBEND
β_x (m)	5.197	5.197	5.200
β_y (m)	2.455	2.458	2.470
η_x (mm)	0.373	0.368	0.355
ν_x	95.111	95.111	95.100
ν_y	35.987	35.980	35.963
Natural ξ_x	-133.6	-133.6	-133.4
Natural ξ_x	-111.4	-111.4	-112.1

lattice is sufficiently flexible that we can compensate for such changes and restore the design working point and lattice parameters. An important goal of our work is to provide a fast model of the APS lattice that includes and corrects for fringe field effects, to facilitate rapid commissioning of the ring.

VI. CONCLUSIONS

We have presented a way to incorporate fringe field effects into hard edge models of general Cartesian dipoles. We have expressed these effects as a map to be applied at the hard edge, and shown the resulting predictions for both transverse gradient dipoles and staircaselike realizations of longitudinal gradient dipoles. In the former case the fringe terms due to the strong focusing fields can completely dominate the usual dipole contributions. Finally, we showed how these models have been incorporated into the tracking code ELEGANT for fast modeling of storage rings including the APS-U.

ACKNOWLEDGMENTS

This work was supported by U.S. Department of Energy Office of Sciences under Contract No. DE-AC02-06CH11357.

APPENDIX A: THE GENERALIZED GRADIENT REPRESENTATION OF A PARALLEL-PLATE DIPOLE

Here we would like to show how our approach relates to the dipole fringe model first worked out in Ref. [4] and described further in [5]. In brief, these references assume that the dipole is effectively infinite along x , which leads to a \mathbf{B} -field that depends only on the dipole field profile, its derivatives, and the vertical coordinate y . Since here we will only compare the field representations, it will be simpler to work with the magnetic potential $\psi(\mathbf{x})$. The skew-free generalized gradient representation of the potential is [14]

$$\psi = \sum_{m=1}^{\infty} \Im[(x + iy)^m] \sum_{\ell=0}^{\infty} \frac{m!(x^2 + y^2)^{\ell} C_m^{[2\ell]}(z)}{(-4)^{\ell} \ell! (m + \ell)!}, \quad (\text{A1})$$

and one can show that the magnetic field $\mathbf{B} = \nabla\psi$ is identical to that found by taking the curl of the vector potential (2)–(4).

A well-made dipole should be symmetric in x which implies that the expansion will be dominated by terms with m odd. Hence, for $m = 2p + 1$ we propose redefining the generalized gradients via

$$p \geq 1: C_{2p+1}(z) \rightarrow S_{2p+1}(z) + \frac{C_1^{[2p]}(z)}{4^p (2p + 1)!}. \quad (\text{A2})$$

This means that all the odd generalized gradients include higher-order derivatives of the on-axis dipole field C_1 . Then, we claim that the expansion (A1) becomes

$$\begin{aligned} \psi &= \sum_{p=0}^{\infty} \frac{(-1)^p y^{2p+1}}{(2p+1)!} C_1^{[2p]}(z) + \sum_{p=1}^{\infty} \mathfrak{S}[(x+iy)^{2p+1}] \\ &\times \sum_{\ell=0}^{\infty} \frac{(2p+1)!(x^2+y^2)^\ell}{(-4)^\ell \ell! (2p+1+\ell)!} S_{2p+1}^{[2\ell]}(z) \\ &+ \sum_{p=1}^{\infty} \mathfrak{S}[(x+iy)^{2p}] \sum_{\ell=0}^{\infty} \frac{(2p)!(x^2+y^2)^\ell}{(-4)^\ell \ell! (2p+\ell)!} C_{2p}^{[2\ell]}(z). \end{aligned} \quad (\text{A3})$$

The first term involves only powers of y and derivatives of the dipole field profile, and results in a magnetic field that is identical to that proposed in [4,5]. In other words, we can reproduce the theory of [4] by first setting all contributions $\sim C_{2p}(z)$ that are antisymmetric in x to zero, and then assuming that the terms proportional to $S_{2p+1}(z)$ also vanish; the latter is equivalent to assuming that the dipole is infinite along x .

Unfortunately, we have been unable to prove that (A2) implies (A3) for all p ; we have, however, used *Mathematica* to verify its validity for $p \leq 9$ ($m \leq 19$); at the very least it is true out to the order of p one is likely to use. When $p = 1$ we have

$$S_3(z) = C_3(z) - \frac{C_1''(z)}{24} = \frac{p_0}{6\rho q B_0} \frac{\partial^2 B_y}{\partial x^2}, \quad (\text{A4})$$

which shows that the curvature term is indeed the first correction encapsulating the finite extent of the dipole. In addition, the expression (A3) may provide a way to quantify higher-order aberrations to the ‘‘pure’’ dipole field.

APPENDIX B: COMPARISON TO PREVIOUS RESULTS

This Appendix compares our fringe field map, which applies at the magnet’s hard edge, to the usual fringe maps at the entrance plane. We will do this assuming that there is no focusing component and that the body sextupole term vanishes, in which case the Cartesian dipole is the same as a sector bend, and our results should match those published previously. We begin with the second-order Taylor map results for the fringe field corrections at the entrance plane given by Refs. [1–3]:

$$\Delta x_e = -\frac{\sec^2 \theta g^2 K_0}{1+\delta} \frac{1}{\rho} - \frac{x_e^2 \sin^2 \theta - y_e^2}{2\rho \cos^2 \theta (1+\delta)}, \quad (\text{B1})$$

$$\begin{aligned} \Delta p_{x,e} &= -\frac{\sec^3 \theta \sin \theta_1 g^2 K_0}{1+\delta} \frac{1}{\rho^2} + \frac{\tan^2 \theta g^2 K_4}{2 \cos \theta \rho R} \\ &+ \frac{\tan \theta}{\rho} x_e - \frac{\tan \theta}{\cos^2 \theta_1} \frac{g K_5}{\rho R} x_e \\ &+ \frac{\tan^2 \theta}{\rho(1+\delta)} (x_e p_{x,e} - y_e p_{y,e}) \\ &+ \frac{K_6}{2\rho R} \frac{y_e^2 - x_e^2}{\cos^3 \theta} + \frac{\tan \theta (2 \tan^2 \theta_1 + 1)}{2\rho^2 (1+\delta)} y_e^2, \end{aligned} \quad (\text{B2})$$

$$\Delta y_e = \frac{\tan^2 \theta_1}{\rho(1+\delta)} x_e y_e, \quad (\text{B3})$$

$$\begin{aligned} \Delta p_{y,e} &= -\frac{\tan \theta}{\rho} y_e + \frac{1 + \sin^2 \theta}{(1+\delta) \cos^3 \theta} \frac{g K_2}{\rho^2} y_e \\ &+ \frac{\tan \theta}{\cos^2 \theta} \frac{g K_5}{\rho R} y_e - \frac{y_e p_{x,e} + x_e p_{y,e} \sin^2 \theta}{\rho \cos^2 \theta (1+\delta)} \\ &+ \sec^3 \theta \frac{K_6}{\rho R} x_e y_e + \frac{2 \cos^2 \theta - 4}{3 \cos^3 \theta (1+\delta)} \frac{K_3}{\rho^2 g} y_e^3. \end{aligned} \quad (\text{B4})$$

We have added the subscript e to all coordinates to indicate that they are defined along the entrance plane of the magnet, namely, the red line in Fig. 2.

To find the fringe field corrections at the hard edge of the magnet, we must map the displaced coordinates at the entrance plane through an ideal bend, and then subtract off what the initial, uncorrected entrance coordinates would be if they merely drifted in vacuum to the hard edge. We do this in the following four steps: (1) Relate the particle coordinates along the entrance plane to the rectangular (x, y, z) coordinate axes oriented along magnet. (2) Map the displaced coordinates along the ideal bending magnet trajectories to the hard edge. (3) Map the initial coordinates with a simple drift to the hard edge. (4) Take the difference of step 3 from step 2 and express everything using hard edge coordinates.

The first step is simple geometry: the vertical coordinates $(y, p_y) = (y_e, p_{y,e})$, while in the horizontal

$$x = x_e \cos \theta, \quad (\text{B5})$$

$$p_x = p_{x,e} \cos \theta + \sqrt{(1+\delta)^2 - p_{x,e}^2 - p_{y,e}^2} \sin \theta. \quad (\text{B6})$$

Step two is resolved using the particle trajectories in a constant bending field $\mathbf{B} = (p_0 c / q \rho) \hat{y}$. A particle with initial coordinates $(x_i, p_{xi}, y_i, p_{yi})$ at z_i has momenta

$$p_x(z) = p_{xi} - (z - z_i) / \rho, \quad (\text{B7})$$

$$p_y(z) = p_{yi}, \quad (\text{B8})$$

and Cartesian coordinates

$$x = x_i + \rho \sqrt{(1 + \delta)^2 - p_x^2(z) - p_{y_i}^2} - \rho \sqrt{(1 + \delta)^2 - p_{x_i}^2 - p_{y_i}^2}, \quad (\text{B9})$$

$$y = y_i - p_{y_i} \rho \tan^{-1} \left[\frac{p_x(z)}{\sqrt{(1 + \delta)^2 - p_x^2(z) - p_{y_i}^2}} \right] + p_{y_i} \rho \tan^{-1} \left[\frac{p_{x_i}}{\sqrt{(1 + \delta)^2 - p_{x_i}^2 - p_{y_i}^2}} \right]. \quad (\text{B10})$$

We want to use the bending magnet trajectories (B7)–(B10) to map the fringe-corrected positions and momenta along the entrance plane of the magnet to the hard edge at $z = 0$. The horizontal positions and momenta are found from inserting (x_i, p_{x_i}) into the left of Eqs. (B5) and (B6) and the displaced edge coordinates into the right; applying similar reasoning to the vertical equations $(y, p_y) = (y_e, p_{y,e})$ yields

$$x_i = (x_e + \Delta x_e) \cos \theta, \quad (\text{B11})$$

$$p_{x_i} \approx (p_{x,e} + \Delta p_{x,e}) \cos \theta + (1 + \delta) \sin \theta - \frac{(p_{x,e} + \Delta p_{x,e})^2 + (p_{y,e} + \Delta p_{y,e})^2}{2(1 + \delta)} \sin \theta, \quad (\text{B12})$$

$$y_i = y_e + \Delta y_e, \quad (\text{B13})$$

$$p_{y_i} = p_{y,e} + \Delta p_{y,e}. \quad (\text{B14})$$

These are located along the entrance plane at the longitudinal position $z_i = -\sin \theta (x_e + \Delta x_e)$. We now insert the initial values (B11)–(B14) into the bending magnet trajectories (B7)–(B10), expand to second order, and find that at the hard edge $z = 0$ we have

$$x(0) \approx \frac{x_e + \Delta x_e}{\cos \theta} \left[1 - \frac{\tan^2 \theta}{2\rho(1 + \delta)} (x_e + \Delta x_e) \right] + \frac{\sec \theta \tan^2 \theta}{(1 + \delta)} (x_e + \Delta x_e) (p_{x,e} + \Delta p_{x,e}), \quad (\text{B15})$$

$$p_x(0) \approx (1 + \delta) \sin \theta + (p_{x,e} + \Delta p_{x,e}) \cos \theta - \sin \theta \frac{x_e + \Delta x_e}{\rho} - \frac{\sin \theta (p_{x,e} + \Delta p_{x,e})^2}{2(1 + \delta)} - \frac{\sin \theta}{2(1 + \delta)} (p_{y,e} + \Delta p_{y,e})^2, \quad (\text{B16})$$

$$y(0) = y_e + \Delta y_e + \frac{\tan \theta}{1 + \delta} (p_{y,e} + \Delta p_{y,e}) (x_e + \Delta x_e), \quad (\text{B17})$$

$$p_y(0) = p_{y,e} + \Delta p_{y,e}. \quad (\text{B18})$$

Combining these with the fringe field displacements listed in Eqs. (B1)–(B4) completes step 2.

Step 3 involves taking the initial coordinates along the entrance plane and drifting them to the hard edge. We computed this in (15)–(20); and expanding to second order shows that

$$x_0 \approx \frac{x_e}{\cos \theta} + \frac{\sec \theta \tan \theta}{1 + \delta} \left(x_e p_{x,e} - \tan \theta_1 \frac{x_e^2}{2\rho} \right), \quad (\text{B19})$$

$$p_{x_0} \approx (1 + \delta) \sin \theta + p_{x,e} \cos \theta - \frac{\sin \theta}{2(1 + \delta)} (p_{x,e}^2 + p_{y,e}^2), \quad (\text{B20})$$

$$y_0 = y_e + \frac{\tan \theta}{1 + \delta} p_{y,e} x_e, \quad (\text{B21})$$

$$p_{y_0} = p_{y,e}. \quad (\text{B22})$$

Alternatively, we could have derived this by setting $\Delta x_e = \Delta p_{x,e} = \Delta y_e = \Delta p_{y,e} = 0$ in the bending magnet Eqs. (B15)–(B18), and taking the $\rho \rightarrow \infty$ limit.

Now, we proceed to step 4 by subtracting the drifted initial values (B19)–(B22) from the full coordinates bent along the magnet trajectories that are given by Eqs. (B15)–(B18). We then complete the calculation by eliminating the entrance plane variables in favor of those at the hard edge by approximately inverting the drift equations as follows

$$x_e \approx x \cos \theta, \quad (\text{B23})$$

$$p_{x,e} \approx p_x / \cos \theta, \quad (\text{B24})$$

$$y_e \approx y - \frac{\tan \theta}{1 + \delta} \frac{p_y x}{\cos \theta}, \quad (\text{B25})$$

$$p_{y,e} = p_y. \quad (\text{B26})$$

After some cancellations we find that the fringe field corrections at the magnet hard edge are given by Eqs. (61)–(64) with $\rho_+ = \rho$, $1/\rho_- = 0$, and $\theta = \theta_{\text{entry}}$. A similar calculation that starts with the exit map of the dipole reproduces our results with $1/\rho_+ = 0$, $\rho_- = \rho$, and $\theta = -\theta_{\text{exit}}$ provided the fringe integrals are properly interpreted (we have defined all integrals to be evaluated along the z axis about $z = z_{\text{edge}}$, while previous references typically compute them from outside to inside the magnet).

APPENDIX C: DERIVATION OF THE SYMPLECTIC FRINGE MAP AND THE PATH LENGTH TERMS

This Appendix provides a brief derivation of the symplectic fringe field map (69)–(85), and includes explicit expressions for the particle path length. The linear part of the fringe field map is generated by

$$\begin{aligned}\Omega_{\text{lin}} = & \frac{\sec^3\theta}{2(1+\delta)} \left(\frac{g^2 K_0}{\rho} \right) p_x + \left[\frac{\tan^2\theta}{2} \left(\frac{g^2 K_4}{R\rho} \right) - \tan\theta \left(1 - \frac{1}{2} \tan^2\theta \right) (g^2 K I_1) \right] x \\ & + \left[- \left(\frac{\tan\theta}{\rho_+} - \frac{\tan\theta}{\rho_-} \right) + \frac{1 + \sin^2\theta}{\cos^3\theta(1+\delta)} \left(\frac{gK_2}{\rho^2} \right) + \left(1 + \frac{1}{2} \tan^2\theta \right) (gKI_0) \right] \frac{y^2}{2} \\ & + \tan\theta \left(\frac{gK_5}{R\rho} \right) \frac{y^2 \sec^2\theta - x^2}{2} - \left(1 - \frac{1}{2} \tan^2\theta \right) (gKI_0) \frac{x^2}{2} + \frac{\sec\theta}{1+\delta} (g^2 KI_0) (p_{y,y} - p_{x,x}),\end{aligned}\quad (\text{C1})$$

while the second order terms arise from a sum of the generators

$$\Omega_2 = \frac{\sec\theta}{1+\delta} \left(\frac{gK_5}{\rho R} \right) p_y x y - \left(\frac{K_6}{R\rho} \right) \frac{x^3}{6} - \frac{\tan\theta}{12} (K_+ - K_-) x^3, \quad (\text{C2})$$

$$\Omega_3 = -\frac{\sec^2\theta}{1+\delta} \left(\frac{1}{\rho_+} - \frac{1}{\rho_-} \right) \frac{p_x y^2}{2} + \frac{\sec^3\theta}{1+\delta} \left(\frac{gK_5}{\rho R} \right) \frac{p_x y^2}{2} - \frac{\tan\theta}{4} (K_+ - K_-) x y^2 + \frac{\sec^2\theta}{2} \left(\frac{K_6}{R\rho} \right) x y^2, \quad (\text{C3})$$

$$\Omega_4 = -\frac{\sec^3\theta}{2(1+\delta)} \left(\frac{gK_5}{\rho R} \right) p_x x^2 - \frac{1 + \sin^2\theta}{\cos^3\theta(1+\delta)} \left(\frac{K_3}{\rho^2} \right) \frac{y^4}{6}. \quad (\text{C4})$$

The total fringe field map can then be approximately split into the sequence

$$e^{:\Omega_M:} = e^{:\Omega_{\text{lin}}:} e^{:\Omega_2:} e^{:\Omega_3:} e^{:\Omega_4:} \approx e^{:\Omega_{\text{lin}}:} e^{:\Omega_2:} e^{:\Omega_3:} e^{:\Omega_4:}, \quad (\text{C5})$$

since all the commutator terms in the Zassenhaus/Baker-Campbell-Hausdorff formula $e^{X+Y} = e^X e^Y e^{-[X,Y]/2} \dots$ are $O(\epsilon^4)$ or higher. Hence, a suitable approximation to the fringe field map can be found by first mapping the coordinates using $e^{:\Omega_{\text{lin}}:}$, then by $e^{:\Omega_2:}$, and so on. We found the linear map using a trial and error and some intuition, while the nonlinear contributions can be obtained exactly using the monomial expressions [26]

$$e^{a:q^n p^m:} q = \begin{cases} q[1 + a(n-m)q^{n-1}p^{m-1}]^{m/(m-n)} & \text{if } n \neq m \\ q \exp(-anq^{n-1}p^{n-1}) & \text{if } n = m \end{cases}, \quad (\text{C6})$$

$$e^{a:q^n p^m:} p = \begin{cases} p[1 + a(n-m)q^{n-1}p^{m-1}]^{n/(n-m)} & \text{if } n \neq m \\ p \exp(anq^{n-1}p^{n-1}) & \text{if } n = m \end{cases}. \quad (\text{C7})$$

Finally, the symplectic fringe field map is completed by including the following updates to the particle path length:

$$\begin{aligned}\ell_1 = & \ell_0 - \frac{P_x}{(1+\delta)^2} p_{x,0} + \frac{1+a-e^a}{a^2(1+\delta)} P_x (ax_0 + X_d) - \frac{a}{1+\delta} (p_{x,0}x_0 - p_{y,0}y_0) + \frac{1+\sin^2\theta}{\cos^3\theta(1+\delta)^2} \left(\frac{gK_2}{\rho^2} \right) \frac{y_0^2}{2} \\ & - \left[\tan\theta \left(\frac{gK_5}{\rho R} \right) + \left(1 - \frac{1}{2} \tan^2\theta \right) (gKI_0) \right] \left[\frac{e^{2a} - 1 - 2a}{4a(1+\delta)} x_0^2 + \frac{(e^a - 1)^2 X_d x_0}{2a^2(1+\delta)^2} + \frac{e^{2a} - 4e^a + 2a + 3}{4a^3(1+\delta)^3} X_d^2 \right] \\ & - \frac{e^{-2a} - 1 + 2a}{4a(1+\delta)} \left[\left(\frac{\tan\theta}{\rho_+} + \frac{\tan\theta}{\rho_-} \right) - \frac{\tan\theta}{\cos^2\theta} \left(\frac{gK_5}{\rho R} \right) - \left(1 + \frac{1}{2} \tan^2\theta \right) (gKI_0) \right] y_0^2,\end{aligned}\quad (\text{C8})$$

followed by

$$\ell_2 = \ell_1 + \frac{\sec\theta}{(1+\delta)^2} \left(\frac{gK_5}{\rho R} \right) p_{y,2} x_2 y_2, \quad (\text{C9})$$

and then

$$\ell_3 = \ell_2 + \frac{\sec^3\theta}{2(1+\delta)^2} \left[\left(\frac{gK_5}{\rho R} \right) - \left(\frac{1}{\rho_+} - \frac{1}{\rho_-} \right) \right] \left\{ p_{x,2} + \left[\sec^2\theta \left(\frac{K_6}{\rho R} \right) - \frac{\tan\theta}{2} (K_+ - K_-) \right] \frac{y_2^2}{4} \right\} y_2^2, \quad (\text{C10})$$

and finally

$$\ell_4 = \ell_3 - \frac{\sec^3\theta}{2(1+\delta)^2} \left(\frac{gK_5}{\rho R} \right) x_3^2 p_{x,3} - \frac{1 + \sin^2\theta}{\cos^3\theta(1+\delta)^2} \left(\frac{K_3}{g\rho^2} \right) \frac{y_3^3}{6}. \quad (\text{C11})$$

-
- [1] K. L. Brown, First and second-order matrix theory for the design of beam transport systems and charged particle spectrometers, SLAC Report No. SLAC-75, 1982.
- [2] L. Sagalovsky, Third-order charged particle beam optics, PhD thesis, University of Illinois at Urbana-Champaign, 1989, Fermilab-thesis-1989-53.
- [3] K. Hwang and S. Y. Lee, Dipole fringe field thin map for compact synchrotrons, *Phys. Rev. ST Accel. Beams* **18**, 122401 (2015).
- [4] G. E. Lee-Whiting, First- and second-order motion through the fringing field of a bending magnet, *Nucl. Instrum. Methods Phys. Res., Sect. A* **294**, 31 (1990).
- [5] E. Forest, *Beam Dynamics: A New Attitude and Framework* (Harwood Academic Publishers, Amsterdam, 1998), Sec. 13.1.
- [6] M. Bassetti and C. Biscari, Analytical formulae for magnetic multipoles, *Part. Accel.* **52**, 221 (1996).
- [7] Y. Cai and Y. Nosochkov, Dynamical effects due to fringe field of the magnet in circular accelerators, SLAC Report No. SLAC-PUB-11181, 2005.
- [8] L. Farvacque *et al.*, A low-emittance lattice for the ESRF, in *Proceedings of the International Particle Accelerator Conference, IPAC'13* (JACoW Publishing, Geneva, Switzerland, 2013), pp. 79–81.
- [9] M. Borland, V. Sajaev, and Y. Sun, Hybrid seven-bend-achromat lattice for the Advanced Photon Source Upgrade, in *Proceedings of International Particle Accelerator Conference, IPAC'15* (JACoW Publishing, Geneva, Switzerland, 2015), pp. 1776–1779.
- [10] A. Streun, T. Garvey, L. Rivkin, V. Schlott, T. Schmidt, P. Willmott, and A. Wrulich, SLS-2—the upgrade of the Swiss Light Source, *J. Synchrotron Radiat.* **25**, 631 (2018).
- [11] J. Delahaye and J. P. Potier, Reverse bending magnets in a combined-function lattice for the CLIC damping ring, in *Proceedings of the Particle Accelerator Conference, PAC'89* (IEEE, New York, NY, 1990), pp. 1611–1613.
- [12] A. Streun, The anti-bend cell for ultralow emittance storage ring lattices, *Nucl. Instrum. Methods Phys. Res., Sect. A* **737**, 148 (2014).
- [13] M. Borland, ELEGANT: A flexible SDDS-compliant code for accelerator simulation, ANL Report No. LS-287, 2000.
- [14] A. J. Dragt, *Lie Methods for Nonlinear Dynamics with Applications to Accelerator Physics* (University of Maryland, College Park, MA, 2019).
- [15] M. Venturini and A. J. Dragt, Accurate computation of transfer maps from magnetic field data, *Nucl. Instrum. Methods Phys. Res., Sect. A* **427**, 387 (1999).
- [16] C. E. Mitchell and A. J. Dragt, Accurate transfer maps for realistic beam-line elements: Straight elements, *Phys. Rev. ST Accel. Beams* **13**, 064001 (2010).
- [17] M. Borland, R. R. Lindberg, and R. Soliday, Tools for use of generalized gradient expansions in accelerator simulations, in *Proceedings of the 9th International Particle Accelerator Conference, Washington, DC, 2021* (JACoW, Geneva, 2021), p. 4500.
- [18] D. Zhou, J. Y. Tang, Y. Chen, and N. Wang, Explicit maps for the fringe field of a quadrupole, in *Proceedings of the 1st International Particle Accelerator Conference, Washington, DC, 2010* (JACoW, Geneva, 2010), p. 4500.
- [19] H. A. Enge, Effect of extended fringing fields on ion-focusing properties of deflecting magnets, *Rev. Sci. Instrum.* **35**, 278 (1964).
- [20] B. D. Muratori, J. K. Jones, and A. Wolski, Analytical expressions for fringe fields in multipole magnets, *Phys. Rev. ST Accel. Beams* **18**, 064001 (2015).
- [21] M. Jaski, J. Liu, A. Jain, C. Spataro, D. J. Harding, V. S. Kashikhin, and M. L. Lopes, Magnet designs for the multi-bend achromat lattice at the advanced photon source, in *Proceedings of the 6th International Particle Accelerator Conference, Richmond, VA, 2015* (JACoW, Geneva, 2015), p. 3260.
- [22] M. Borland, Symplectic integration in elegant, Advanced Photon Source Technical Report No. LS-356, 2021.
- [23] E. Forest, Canonical integrators as tracking codes, *AIP Conf. Proc.* **184**, 1106 (1989).
- [24] H. Yoshida, Construction of higher order symplectic integrators, *Phys. Lett. A* **150**, 262 (1990).
- [25] E. Forest and R. Ruth, Fourth-order symplectic integration, *Physica D (Amsterdam)* **43**, 105 (1990).
- [26] I. Gjaja, Monomial factorization of symplectic maps, *Part. Accel.* **43**, 133 (1994).